J. Fluid Mech. (2025), *vol*. 1002, A9, doi:10.1017/jfm.2024.1140

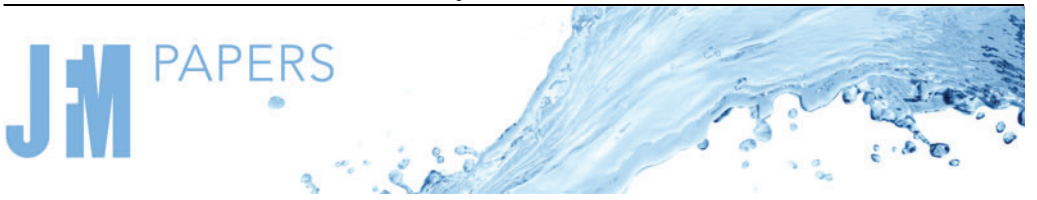

Mechanisms underlying how free surfaces influence very-large-scale motions in turbulent plane open channel flows based on linear non-modal analysis

Bing-Qing Deng[1], **Zixuan Yang**[2] **and Lian Shen**[3],†

[1]School of Engineering Science, University of Chinese Academy of Sciences, Beijing 101408, PR China

[2]Institute of Mechanics, Chinese Academy of Sciences, Beijing 100190, PR China

[3]Department of Mechanical Engineering and St. Anthony Falls Laboratory, University of Minnesota, Minneapolis, MN 55455, USA

(Received 31 May 2024; revised 20 November 2024; accepted 21 November 2024)

Linear non-modal analyses are performed to study the mechanism of how deformable free surfaces influence very-large-scale motions (VLSMs) in turbulent open channel flows. The mean velocity and eddy viscosity profiles obtained from direct numerical simulations are used in the generalised Orr–Sommerfeld and Squire equations to represent background turbulence effects. Solutions of surface-wave eigenmodes and shear eigenmodes are obtained. The results indicate that at high Froude numbers, free surfaces enhance the maximum transient growth rate of VLSMs through surface-wave eigenmodes. We then analyse the energy budget equation to reveal the underlying mechanism. For streamwise-uniform motions, the energy growth rate is enhanced by an energy production term associated with the correlation between the streamwise velocity, which is generated by the lifting-up effect of streamwise vortices composed of shear eigenmodes, and the vertical velocity, which is induced by a spanwise standing wave composed of surface-wave eigenmodes. For streamwise-varying motions, the energy growth rate is enhanced by a standing wave moving with a pair of vortices that travel at a speed approximately equal to the projection of the mean surface velocity along the wavenumber vector direction. Finally, an analytical expression of the energy production term is derived to provide the initial conditions for the maximum transient growth and explain the weak free-surface effect observed at large spanwise wavenumbers and low Froude numbers. The results

† Email address for correspondence: shen@umn.edu

demonstrate a linear non-modal mechanism in interactions between free surfaces and VLSMs in open channel flows.

Key words: wave–turbulence interactions, channel flow, turbulent boundary layers

1. Introduction

Flows in shallow open waters, such as continental shelves, rivers and channels, are characterised by turbulent shear flows with a free surface at the top. Research on turbulent flows in open channels is important for various applications, such as remote monitoring, environmental protection, aquaculture and river hydraulic engineering. Turbulent flows impinging on free surfaces can lead to surface deformation, which is a basis for non-invasive monitoring of underwater currents (Nichols *et al.* 2013; Legleiter, Mobley & Overstreet 2017). Moreover, the kinematic and dynamic boundary conditions of the free surface can constrain and distort turbulent motions, which control the transport of dissolved gases, pollutants and sediment in water (Hunt 1984; Jähne & Haußecker 1998). Research on the effects of free surfaces on turbulent motions in open channel flows aiming at elucidating the fundamental mechanisms underlying interactions between free surfaces and turbulence is crucial for providing a theoretical basis for developing turbulence models in various applications.

For turbulent flows under free surfaces, the Froude number $u^*/\sqrt{gl^*}$ is a key parameter that determines free surface deformation and turbulent flow properties, with u^* being the characteristic velocity and l^* being the characteristic length scale. It has been found that the effect of free surfaces can extend from the near-surface region to the bulk region as the Froude number increases. At low Froude numbers, the free surface mainly modulates turbulence eddies in the source layer near the surface (Rashidi & Banerjee 1988; Leighton *et al.* 1991; Handler *et al.* 1993; Komori, Nagaosa & Murikami 1993; Borue, Orszag & Staroselsky 1995; Shen *et al.* 1999), where the turbulence becomes anisotropic due to the constraint of the free surface vertical motions (Hunt & Graham 1978; Shen *et al.* 1999; Calmet & Magnaudet 2003). Yoshimura & Fujita (2020) performed direct numerical simulations and compared turbulence intensity in open channel flows at relatively high Froude numbers and in closed channel flows. They found that the intensity of streamwise velocity fluctuations in the outer layer increases slightly as the Froude number increases. Based on direct numerical simulations at low Reynolds numbers, Di *et al.* (2019) reported an increase in the energy spectrum of streamwise velocity fluctuations at low streamwise wavenumbers (with the corresponding length scale longer than six times the water depth) in the outer layer as the Froude number increases. Duan *et al.* (2020) conducted laboratory experiments at moderate Reynolds numbers and found that the streamwise velocity fluctuations in the outer layer, approximately one hundred wall units above the wall, are larger in open channel flows with a deformable free surface than in closed channel flows. This result was attributed to the amplification of the intensity of very-large-scale streamwise velocity fluctuations, which have a streamwise length scale approximately twenty times the water depth. These findings indicate that an increase in the Froude number can lead to an increase in the intensity of very-large-scale streamwise velocity fluctuations in the outer layer of open channel flows. The underlying mechanisms are the subject of our study.

The length scale of the turbulent motions enhanced by the presence of a free surface is consistent with that of very-large-scale motions (VLSMs) observed in the outer layer of wall-bounded turbulent flows. Specifically, in open channel flows, the streamwise length

scale of VLSMs is typically of the order of ten times the water depth (Cameron, Nikora & Stewart 2017; Wang & Richter 2019; Duan *et al.* 2020; Peruzzi *et al.* 2020; Zampiron, Cameron & Nikora 2020; Pinelli *et al.* 2022), although it is influenced by the aspect ratio in open channel flows with sidewalls (Peruzzi *et al.* 2020; Zampiron *et al.* 2020). This length scale can be identified according to one of the distinct peaks in the bimodal distribution of the pre-multiplied streamwise energy spectrum of streamwise velocity fluctuations within the outer layer (Hutchins & Marusic 2007; Monty *et al.* 2007; Marusic, Mathis & Hutchins 2010). VLSMs are known to emerge under moderate to high Reynolds numbers (Hutchins & Marusic 2007), while the Reynolds numbers needed for generating VLSMs in open channels are much lower than those required in closed channels (Wang & Richter 2019; Duan *et al.* 2020; Peruzzi *et al.* 2020; Pinelli *et al.* 2022). For open channel flows with sidewalls, VLSMs are observed when the friction Reynolds number is greater than 614 for a smooth bed (Duan *et al.* 2020) and greater than 442 for a rough bed (Shen, Yang & Liu 2023). In recent direct numerical simulations of a plane open channel flow (without sidewalls) in a large computational domain, a weak peak located around $10h$ can also be observed in the pre-multiplied streamwise energy spectrum of the streamwise velocity fluctuations even when the friction Reynolds number is as low as 200, and the spectral peak representing VLSMs becomes clear at the friction Reynolds number 365 (Pinelli *et al.* 2022). Notably, in free-surface open channel flows, the amplification of turbulent motions with length scales comparable with those of VLSMs has been observed at relatively low and moderate Reynolds numbers. Hence, to discuss the effect of free surfaces on underwater turbulent motions (and *vice versa*), we broaden the scope of 'VLSMs' to include motions with length scales similar to those of VLSMs, removing the conventional restrictions of high Reynolds numbers in canonical wall-bounded turbulence.

VLSMs play an important role in momentum transfer in the outer layer of wall-bounded turbulent flows and have therefore attracted considerable attention (Kim & Adrian 1999; Guala, Hommema & Adrian 2006; Hutchins & Marusic 2007; Marusic *et al.* 2010). VLSMs manifest as low-speed streaks of streamwise velocity fluctuations and a hierarchy of hairpin vortex packets (Adrian & Marusic 2012). VLSMs contribute to more than 50 % of the streamwise velocity fluctuations and Reynolds shear stress in the outer layer of turbulent open channel flows at moderate Reynolds numbers (Duan *et al.* 2020), similar to observations in pipe flows and closed channel flows (Guala *et al.* 2006; Balakumar & Adrian 2007; Monty *et al.* 2007). Distinctly, VLSMs in free-surface open channel flows markedly influence the Reynolds shear stress near the free surface (Duan *et al.* 2020; Peruzzi *et al.* 2020), which differs from their counterparts in flat-plate boundary layers, closed channel flows and pipe flows (Guala *et al.* 2006; Hutchins & Marusic 2007; Monty *et al.* 2007). This notable intensity of VLSMs near the free surface can be linked to the impingement of hairpin vortices originating from the near-wall region on the surface (Nakagawa & Nezu 1977; Rashidi & Banerjee 1988; Gulliver & Halverson 1989; Nezu & Nakagawa 1997; Rashidi 1997; Tamburrino & Gulliver 2007), leading to surface signatures characterised by low-speed streak patterns (Lam & Banerjee 1992; Rashidi 1997; Tamburrino & Gulliver 2007; Cameron *et al.* 2017). Consequently, VLSMs can significantly impact surface renewal processes and scalar transport across free surfaces (Rashidi & Banerjee 1988; Komori, Murakami & Ueda 1989; Rashidi 1997; Pinelli *et al.* 2022).

Given the importance of VLSMs, as reviewed above, it is worth exploring the mechanism underlying the amplification of VLSMs with increasing Froude numbers in free-surface open channel flows. In this paper, we use the term 'free-surface open channel' to denote the case with a deformable free surface, as opposed to the 'rigid-lid open channel' case, in which the top boundary is a flat free-slip surface. We also note that it

is widely recognised that interactions between externally generated waves and sheared currents in open channel flows lead to the formation of Langmuir-type cells exhibiting length scales comparable with those of VLSMs and intensities stronger than those of VLSMs in canonical wall-bounded turbulence (Gargett *et al.* 2004; Tejada-Martínez & Grosch 2007; Tejada-Martínez *et al.* 2013; Deng *et al.* 2019; Shrestha *et al.* 2019; Deng *et al.* 2020; Peruzzi *et al.* 2021). The Craik–Leibovich mechanism (Craik & Leibovich 1976; Leibovich 1977) attributes the development of Langmuir-type cells to the vortex force that results from the Stokes drift of water waves interacting with the vorticity. However, the waves occurring in free-surface open channel flows (Dolcetti *et al.* 2016; Yoshimura & Fujita 2020) are significantly weaker than the externally generated waves that lead to the generation of Langmuir-type cells (Gargett *et al.* 2004; Tejada-Martínez & Grosch 2007; Tejada-Martínez *et al.* 2013; Deng *et al.* 2019; Peruzzi *et al.* 2021); thus, the Craik–Leibovich mechanism is not suitable under these conditions. Consequently, further research is needed to investigate how the free surface enhances VLSMs in open channel flows.

In canonical wall-bounded turbulence, the generation of VLSMs is linked to a self-sustaining cycle involving VLSMs and large-scale motions (LSMs) (Cossu & Hwang 2017). This cycle encompasses three processes: the generation of streaks via the linear lift-up effect driven by streamwise vortices, the meandering of streaks through streak instability and/or transient growth, and the subsequent regeneration of streamwise vortices by nonlinear vortex stretching (Hwang & Bengana 2016). Cossu & Hwang (2017) confirmed that very-large-scale streaks can self-sustain by drawing energy directly from the mean flow using the linear non-modal analysis. Based on the very-large-scale streaks obtained by Cossu & Hwang (2017), de Giovanetti, Sung & Hwang (2017) further discovered that LSMs are generated by the linear instability of very-large-scale streaks in the outer region. In open channel flows, Camporeale *et al.* (2021) found that the linear instability induced by secondary currents occurs at the length scales of LSMs, suggesting that the generation mechanisms of LSMs in open channel flows are similar to those in canonical wall-bounded turbulence. However, few studies have been conducted on the free-surface effect on the linear lift-up process responsible for the generation of very-large-scale streaks.

The linear transient growth analysis has been found to be a useful tool for investigating the linear lift-up process responsible for the generation of streaks in wall-bounded turbulence (Butler & Farrell 1993; del Álamo & Jiménez 2006; Cossu, Pujals & Depardon 2009; Pujals *et al.* 2009; Hwang & Cossu 2010). Transient growth refers to the increase in the perturbation energy, even for stable flows, induced by the non-normality of the linearised Navier–Stokes operator (Trefethen *et al.* 1993; Schmid & Henningson 2001; Schmid 2007). del Álamo & Jiménez (2006) and Pujals *et al.* (2009) derived the generalised Orr–Sommerfeld and Squire equations based on the mean velocity and eddy viscosity profiles representing the effects of background turbulent fluctuations. Although the perturbation in the transient growth analysis is small, the linear lift-up effect responsible for the linear transient growth works well for perturbation in turbulence (Jimenez 2018). The generalised Orr–Sommerfeld and Squire equations have been used to study the response of turbulent flows to various boundary conditions (Cossu *et al.* 2009; Willis, Hwang & Cossu 2010; Deng *et al.* 2013; Song *et al.* 2015; Song, Huang & Xu 2017) and predict turbulence statistics in canonical wall-bounded turbulence (Illingworth, Monty & Marusic 2018). Regarding free-surface open channel flows, most of the previous linear stability analyses and non-modal analyses were performed based on the original Orr–Sommerfeld and Squire equations or the Rayleigh equation, and these works focused on the stability of streamwise-propagating surface waves in laminar base flows (Burns

1953; Yih 1972; Triantafyllou & Dimas 1989; Dimas & Triantafyllou 1994; Olsson & Henningson 1995; Ambrosi & Onorato 2008; Samanta 2020). Essentially, these studies investigated the transition from laminar flows to turbulent flows. To investigate the mechanism underlying how the free surface enhances VLSMs in fully developed turbulent open channel flows, there is a need to perform the non-modal transient growth analyses of turbulence in free-surface open channels based on the generalised Orr–Sommerfeld and Squire equations.

In this study, we perform a non-modal transient growth analysis based on the generalised Orr–Sommerfeld and Squire equations to study the transient growth in plane open channel flows with deformable free surfaces. We focus on the length scales where the transient growth rate is influenced by the free surface and study the underlying mechanisms, providing an explanation for the impact of free surfaces on underneath turbulent motions in open channel flows. The reminder of this paper is structured as follows. The mathematical formulation and computational method are introduced in § 2. In § 3, the transient growth rates are compared among cases with different Froude numbers to illustrate the effect of the free surface on turbulent motions. Then, the key mechanisms responsible for the increase in the transient growth rate due to the free surface are examined in § 4. Both streamwise-uniform and streamwise-varying motions are studied. The variation in the free-surface effect with the Froude number and wavenumber is also investigated at three different Reynolds numbers. Finally, the conclusions are given in § 5.

2. Mathematical formulation and computational method

We consider an incompressible viscous flow driven by a constant streamwise pressure gradient in a free-surface open channel. Because this study focuses on the free-surface effect, we employ plane open channel flows to exclude the influence of sidewalls on turbulent motions through secondary currents (Peruzzi *et al.* 2020; Zampiron *et al.* 2020). As depicted in figure 1, the plane open channel flow driven by a pressure gradient is periodic and statistically homogeneous in the streamwise and spanwise directions. This is a simplified model widely used in numerical studies to investigate free-surface effects (Komori *et al.* 1993; Borue *et al.* 1995; Pan & Banerjee 1995; Wang & Richter 2019; Pinelli *et al.* 2022). Following the rationales of previous linear non-modal analyses in canonical wall-bounded turbulence (Reynolds & Hussain 1972; Butler & Farrell 1992; del Álamo & Jiménez 2006; Pujals *et al.* 2009), the linear transient growth of the small-magnitude perturbations $\boldsymbol{u} = (u, v, w)$, p and η in a mean flow with $\boldsymbol{U} = (U(y), 0, 0)$ is studied to investigate the influence of the free surface. Here, u (or u_1), v (or u_2) and w (or u_3) are the velocity perturbations in the streamwise (x or x_1), vertical (y or x_2) and spanwise (z or x_3) directions, p is the disturbed pressure, and η is the surface height perturbation with respect to the mean surface height $y = h$.

2.1. *Linearised equations and boundary conditions*

The perturbations $\boldsymbol{u}$ and p satisfy the continuity equation

$$\boldsymbol{\nabla} \cdot \boldsymbol{u} = 0 \tag{2.1}$$

and the linearised momentum equation (Pujals *et al.* 2009)

$$\frac{\partial \boldsymbol{u}}{\partial t} + U\frac{\partial \boldsymbol{u}}{\partial x} + \left(vU', 0, 0\right) = -\boldsymbol{\nabla} p + \boldsymbol{\nabla} \cdot \left(\nu_T \left(\boldsymbol{\nabla}\boldsymbol{u} + \boldsymbol{\nabla}\boldsymbol{u}^{\mathrm{T}}\right)\right). \tag{2.2}$$

The total viscosity ν_T is equal to the sum of the molecular viscosity ν and the turbulent eddy viscosity ν_t, which varies in the vertical direction. Hereinafter, the superscripts '′' and

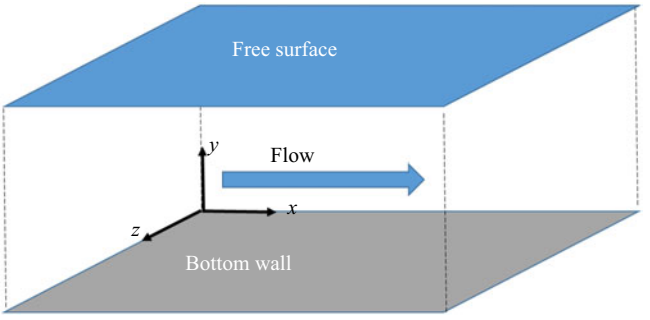

Figure 1. Sketch of free-surface open channel flows without sidewalls. The flow is periodic and homogenous in the streamwise (x) and spanwise (z) directions.

'$\prime\prime$' indicate the first- and second-order derivatives in the vertical direction, respectively. The superscript 'T' represents the transpose of vectors and matrices.

Because the free surface is a material surface, η satisfies the kinematic boundary condition (Mei, Stiassnie & Yue 2005)

$$\frac{\partial \eta}{\partial t} + (U+u)\frac{\partial \eta}{\partial x} + w\frac{\partial \eta}{\partial z} = v, \quad \text{at } y = h + \eta. \tag{2.3}$$

In the present study, the pressure and shear stress imposed at the surface by the air are zero, and the surface tension is negligible, as we focus on VLSMs. Therefore, the perturbations satisfy the following free-surface dynamic boundary conditions:

$$\boldsymbol{n}\cdot\boldsymbol{\sigma}\cdot\boldsymbol{n} = 0, \quad \boldsymbol{t_1}\cdot\boldsymbol{\sigma}\cdot\boldsymbol{n} = 0, \quad \boldsymbol{t_2}\cdot\boldsymbol{\sigma}\cdot\boldsymbol{n} = 0, \quad \text{at } y = h + \eta. \tag{2.4}$$

In (2.4), the first equation represents the equilibrium of the normal stress, and the second and third equations respectively represent the balance of the shear stresses in the tangential directions $\boldsymbol{t_1}$ and $\boldsymbol{t_2}$. The stress tensor $\boldsymbol{\sigma}$ is defined as $(-p - P + gy)\boldsymbol{I} + \nu(\boldsymbol{\nabla}(\boldsymbol{U}+\boldsymbol{u}) + \boldsymbol{\nabla}(\boldsymbol{U}^{\mathrm{T}} + \boldsymbol{u}^{\mathrm{T}}))$, where $\boldsymbol{I}$ is the identity matrix, P is the mean pressure and g is the gravitational acceleration. The unit vectors $\boldsymbol{n}$, $\boldsymbol{t_1}$ and $\boldsymbol{t_2}$ are expressed as

$$\boldsymbol{n} = \frac{(-\partial\eta/\partial x,\, 1,\, -\partial\eta/\partial z)}{\sqrt{(\partial\eta/\partial x)^2 + 1 + (\partial\eta/\partial z)^2}}, \quad \boldsymbol{t_1} = \frac{(1,\, \partial\eta/\partial x,\, 0)}{\sqrt{(\partial\eta/\partial x)^2 + 1}}, \quad \boldsymbol{t_2} = \frac{(0,\, \partial\eta/\partial z,\, 1)}{\sqrt{(\partial\eta/\partial z)^2 + 1}}. \tag{2.5a–c}$$

Substituting the Taylor series of the perturbations $\boldsymbol{u}$ and p at $y = h$ into (2.3)–(2.4) and retaining the first-order terms of η, the free-surface boundary conditions (2.3)–(2.4) are linearised as

$$\frac{\partial \eta}{\partial t} + U\frac{\partial \eta}{\partial x} = v, \tag{2.6}$$

$$-p + g\eta = 2\nu\left(U'\eta_x - \frac{\partial v}{\partial y}\right), \tag{2.7}$$

$$\frac{\partial u}{\partial y} + \frac{\partial v}{\partial x} = -U''\eta, \tag{2.8}$$

$$\frac{\partial w}{\partial y} + \frac{\partial v}{\partial z} = 0, \tag{2.9}$$

at $y = h$. The bottom is a no-slip wall, i.e. $\boldsymbol{u} = 0$ at $y = 0$.

By eliminating the pressure term in (2.2) using the continuity equation (2.1), the generalised Orr–Sommerfeld and Squire equations for the vertical velocity v and vertical vorticity ω_y can be obtained (Schmid & Henningson 2001). We assume that the perturbations in turbulent open channel flows have wave-like forms, i.e.

$$(v, \omega_y, \eta) = \left(\hat{v}(y), \hat{\omega}_y(y), \hat{\eta}\right) \exp(\mathrm{i}(\alpha x + \beta z - \lambda t)) + \text{c.c.}, \tag{2.10}$$

where c.c. is the complex conjugation. The generalised Orr–Sommerfeld and Squire equations in the spectral space can be written as

$$-\mathrm{i}\lambda(\mathrm{D}^2 - k^2)\hat{v} = L_{OS}\hat{v}, \tag{2.11}$$

$$-\mathrm{i}\lambda\hat{\omega}_y = -\mathrm{i}\beta U'\hat{v} + L_{SQ}\hat{\omega}_y. \tag{2.12}$$

Hereinafter, λ is a complex eigenvalue and $k^2 = \alpha^2 + \beta^2$, where α and β are the wavenumbers in the streamwise and spanwise directions, respectively. The notation D denotes the vertical derivative of the perturbations. The coupling term $-\mathrm{i}\beta U'\hat{v}$ is an important source of the non-orthogonality of the linearised equations. This coupling term leads to the generation of the elongated streaks in the streamwise direction, represented by the vertical vorticity in wall-bounded turbulence, through the interaction between the shear of the base flow and the spanwise-varying vertical velocity, which is known as the 'lifting-up' effect (Ellingsen & Plam 1975). The operators L_{OS} and L_{SQ} are expressed as (Pujals *et al.* 2009)

$$L_{OS} = -\mathrm{i}\alpha[U(\mathrm{D}^2 - k^2) - U''] + \nu_T(\mathrm{D}^2 - k^2)^2 + 2\nu_T'(\mathrm{D}^3 - k^2\mathrm{D}) + \nu_T''(\mathrm{D}^2 + k^2), \tag{2.13}$$

$$L_{SQ} = -\mathrm{i}\alpha U + \nu_T(\mathrm{D}^2 - k^2) + \nu_T'\mathrm{D}. \tag{2.14}$$

The linearised free-surface boundary conditions at $y = h$ in (2.6)–(2.9) can be rewritten as

$$-\mathrm{i}\lambda\hat{\eta} + \mathrm{i}\alpha U\hat{\eta} = \hat{v}, \tag{2.15}$$

$$[-\mathrm{i}\lambda + \mathrm{i}\alpha U - \nu_T(\mathrm{D}^2 - k^2) + 2\nu k^2]\mathrm{D}\hat{v} = [\mathrm{i}\alpha U' + \nu_T'(\mathrm{D}^2 + k^2)]\hat{v} + (-g + 2\mathrm{i}\nu\alpha U')k^2\hat{\eta}, \tag{2.16}$$

$$-(\mathrm{D}^2 + k^2)\hat{v} = -\mathrm{i}\alpha\hat{\eta}U'', \tag{2.17}$$

$$\mathrm{D}\hat{\omega}_y = \mathrm{i}\beta\hat{\eta}U''. \tag{2.18}$$

The above linearised free-surface boundary conditions can regress to the rigid free-slip lid conditions ($\eta = 0$) for infinitely small Froude numbers $Fr_\tau \to 0$. In the present study, the friction Froude number Fr_τ is defined based on the friction velocity u_τ at the bottom wall, h and g as $Fr_\tau = u_\tau/\sqrt{gh}$. The no-slip boundary conditions expressed by $\hat{v}$ and $\hat{\omega}_y$ at $y = 0$ are

$$\hat{v} = \hat{\omega}_y = 0. \tag{2.19}$$

Compared with the linear transient growth analysis of laminar flows in free-surface open channels conducted by Olsson & Henningson (1995), we consider turbulence effects, including the mean velocity of the turbulent flow and the eddy viscosity induced by background turbulence. Because the mean velocity is relatively insensitive to the Froude number (Yoshimura & Fujita 2020), the mean velocity profile $U(y)$ in an open channel with a rigid-lid surface is selected as the base flow. We mainly consider four friction Reynolds numbers $Re_\tau = 180$, 360, 1000 and 6000. The friction Reynolds number is defined as $Re_\tau = u_\tau h/\nu$, where u_τ is the friction velocity at the bottom wall. The mean

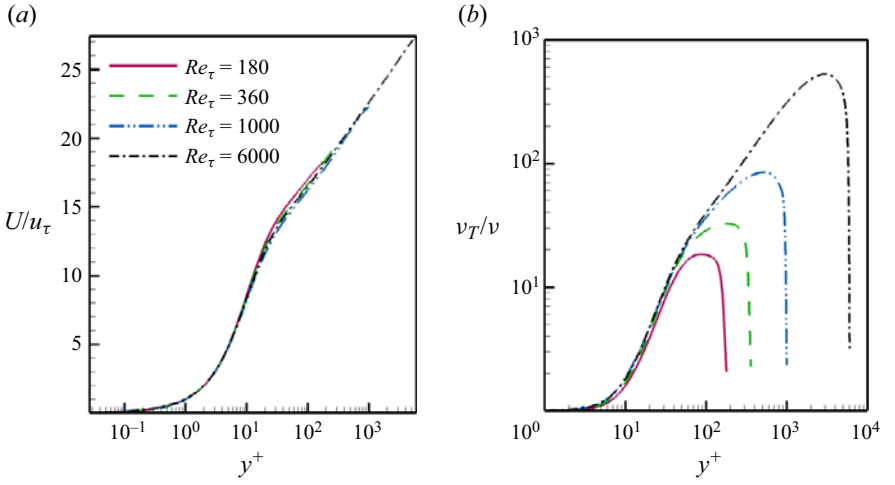

Figure 2. Profiles of the mean velocity U and the total viscosity ν_T at $Re_\tau = 180$, 360, 1000 and 6000.

velocity and total viscosity profiles at $Re_\tau = 180$, 360 and 1000 are obtained using direct numerical simulations based on a spectral and finite-differential method (Kermani *et al.* 2011). The mean velocity and the eddy viscosity at $Re_\tau = 6000$ are obtained using the data from Pirozzoli (2023). The profiles of the mean velocity U and total viscosity ν_T are depicted in figure 2. The non-zero ν_T at the free surface is calculated using L'Hôpital's rule (Shen, Triantafyllou & Yue 2000). The distributions of U and ν_T are similar to those shown by Borue *et al.* (1995). The surface mean velocity and bulk total eddy viscosity increase with increasing Reynolds number. However, ν_T in the outer layer of open channel flows is much smaller than what is determined by the Cess expression in closed channel flows (Pujals *et al.* 2009). Therefore, similar to the linear non-modal analysis in turbulent Couette flow conducted by Hwang & Cossu (2010), we use the U and ν_T profiles obtained from the direct numerical simulations, instead of the Cess expression, in our transient analyses below.

In our studies, we mainly consider four friction Froude numbers $Fr_\tau = 0$, 0.05, 0.1 and 0.142. The corresponding bulk Froude numbers Fr_b, defined based on the bulk mean velocity U_m as $Fr_b = U_m/\sqrt{gh}$, at different Reynolds numbers are listed in table 1. According to Brocchini & Peregrine (2001), wave breaking in open shallow waters primarily occurs when the turbulent Froude number, defined as $F_{BP} = q/\sqrt{2gL}$, exceeds 0.225. In their work, q represents the turbulent intensity near the water surface, and L is the length scale of the most energetic turbulent motion near the surface. The two Froude numbers Fr_τ and F_{BP} satisfy the relation $Fr_\tau = F_{BP}\sqrt{2L/h}(u_\tau/q)$. In open channel flows, the turbulent intensity q is close to u_τ, and $L \approx 1$–$10h$ (Pirozzoli 2023), leading to $Fr_\tau = 1.412F_{BP}$–$4.47F_{BP}$. Consequently, surface breaking typically occurs for $Fr_\tau > 0.312$. It has also been observed in laboratory experiments (Auel, Albayrak & Boes 2014) that no air entrainment or wave breaking occurred even for the bulk Froude number $Fr_b = 3.5$. Thus, for plane open channel flows, the Froude numbers used in the present study (table 1) are below the threshold for breaking free surfaces.

Re_τ	180			360			1000			6000		
Fr_τ	0.05	0.1	0.142	0.05	0.1	0.142	0.05	0.1	0.142	0.05	0.1	0.142
Fr_b	0.78	1.56	2.21	0.86	1.73	2.45	0.98	1.96	2.79	1.23	2.46	3.49

Table 1. Friction Froude number Fr_τ and the corresponding bulk Froude number Fr_b at Reynolds numbers $Re_\tau = 180$, 360, 1000 and 6000 considered in the present study.

2.2. *Computation method for the transient growth rate*

The energy growth rate for the non-dimensional wavenumber $(\alpha h, \beta h)$ is defined as

$$G(\alpha h, \beta h, t) = \sup_{E^{in} \neq 0} \frac{E(\alpha h, \beta h, t)}{E^{in}}. \tag{2.20}$$

Here, E is the total energy, which is defined as

$$E(\alpha h, \beta h, t) = \underbrace{\frac{1}{2k^2}\int_0^h \left(\mathrm{D}\hat{v}(\mathrm{D}\hat{v})^* + k^2\hat{v}\hat{v}^* + \hat{\omega}_y(\hat{\omega}_y)^*\right)\mathrm{d}y}_{E_K} + \underbrace{\frac{1}{2}g\hat{\eta}\hat{\eta}^*}_{E_\eta} = \boldsymbol{q}^*\boldsymbol{M}\boldsymbol{q}. \tag{2.21}$$

In the above equation, E_K is the kinetic energy and E_η is the potential energy. For the vector $\boldsymbol{q} = (\hat{v}, \hat{\omega}_y, \hat{\eta})^{\mathrm{T}}$, the superscript '$*$' indicates the conjugated transpose of a vector or a matrix. The energy matrix $\boldsymbol{M}$ is an operator to compute the energy of the vector $\boldsymbol{q}$. As analysed below in § 4, energy is transformed between E_K and E_η. Therefore, only the growth rate of the total energy E is meaningful from the viewpoint of energy conservation. The superscript '*in*' refers to the initial energy at $t = 0$. The symbol '*sup*' indicates the supremum.

The total energy can be expressed by the eigenmodes $\bar{\boldsymbol{q}}$ and eigenvalues λ of the linearised system (2.11)–(2.19). Assume an expansion of $\boldsymbol{q}$ using the eigenmodes, $\boldsymbol{q}(t) = \boldsymbol{S}\boldsymbol{\kappa}(t)$, in which the columns of matrix $\boldsymbol{S}$ are the eigenmode $\bar{\boldsymbol{q}}$. The parameter vector $\boldsymbol{\kappa}(t)$ satisfies

$$\boldsymbol{\kappa}(t) = \exp(-\mathrm{i}\Lambda t)\,\boldsymbol{\kappa}(t=0), \tag{2.22}$$

in which the diagonal elements of the diagonal matrix Λ are the eigenvalues λ. Therefore,

$$\boldsymbol{q}(t) = \boldsymbol{S}\exp(-\mathrm{i}\Lambda t)\,\boldsymbol{\kappa}(t=0). \tag{2.23}$$

Decompose the Hermitian energy matrix $\boldsymbol{M}$ into $\boldsymbol{M} = \boldsymbol{F}^*\boldsymbol{F}$, and then the total energy in (2.21) can be further written as

$$E(\alpha h, \beta h, t) = \|\boldsymbol{F}\boldsymbol{S}\exp(-\mathrm{i}\Lambda t)\,\boldsymbol{\kappa}(t=0)\|_2^2. \tag{2.24}$$

Here, $\|\,\|_2$ represents the 2-norm of the matrix. Then, the energy growth rate can be expressed as (Schmid & Henningson 2001)

$$G(\alpha h, \beta h, t) = \sup_{E^{in} \neq 0} \|\boldsymbol{F}\boldsymbol{S}\exp(-\mathrm{i}\Lambda t)\,\boldsymbol{S}^{-1}\boldsymbol{F}^{-1}\|_2^2 = \|\boldsymbol{A}\|_2^2. \tag{2.25}$$

The value of $G(\alpha h, \beta h, t)$ and the corresponding initial and amplified perturbations are solved by the singular value decomposition of the matrix $\boldsymbol{\Theta}^*\boldsymbol{A}\boldsymbol{\Upsilon} = \boldsymbol{\Xi}$. The elements of the diagonal matrix $\boldsymbol{\Xi}$ are the singular values of $\boldsymbol{A}$. Here, $G(\alpha h, \beta h, t)$ is equal to the

largest singular value, and the initial and amplified perturbations are the corresponding columns of the unitary matrices $\boldsymbol{\Theta}$ and $\boldsymbol{\Upsilon}$, respectively.

The eigenmodes $\bar{\boldsymbol{q}}$ and eigenvalues λ of the linearised system (2.11)–(2.19) are solved using a Chebyshev spectral collocation method on a grid of $N_y + 1$ collocation points. The real part of the eigenvalue, λ_r, represents the frequency of the perturbation, and λ_r/k represents the advection velocity of the perturbation along the direction of $(\alpha h, \beta h)$. The imaginary part λ_i indicates the temporal stability of the system. The system is unstable if λ_i is positive. In the present study, $N_y = 96$, 128, 192 and 384 are used for $Re_\tau = 180$, 360, 1000 and 6000, respectively. The convergence of the results has been validated by doubling N_y. The code has been validated in our previous study in closed channel flows (Deng *et al.* 2013).

The maximum transient growth rate for the non-dimensional wavenumber $(\alpha h, \beta h)$ is

$$G_{max}(\alpha h, \beta h) = \max_t G(\alpha h, \beta h, t) = G(\alpha h, \beta h, t_{max}), \tag{2.26}$$

where t_{max} represents the instant at which the maximum transient growth rate is obtained. In the non-modal analyses of canonical wall-bounded turbulence (del Álamo & Jiménez 2006; Cossu *et al.* 2009; Pujals *et al.* 2009; Willis *et al.* 2010; Song *et al.* 2015, 2017), the amplified perturbations corresponding to G_{max} have been shown to include the most energetic turbulent motions to a certain extent, and the initial perturbations can provide the conditions for generating these turbulent motions. Moreover, the variance in G_{max} serves as an indicator to assess the difference in the intensities among these turbulent motions.

3. Impact of the free surface on linear transient growth and stability

In this section, the effect of the free surface is first studied by comparing the transient growth rate at different Froude numbers, and then the influence of the free surface on the stability is discussed.

3.1. *Transient growth rate in free-surface open channel flows*

Figure 3 compares the contours of the maximum transient growth rate $G_{max}(\alpha h, \beta h)$ at $Fr_\tau = 0.05$, 0.1 and 0.142 with that at $Fr_\tau = 0$ (rigid free-slip lid case) for $Re_\tau = 180$. The transient growth mainly occurs in the region of $\alpha h < \beta h$. For any given spanwise wavenumber βh, G_{max} increases as the streamwise wavenumber αh decreases, reaching its maximum value at $\alpha h = 0$. These two features are similar to those observed in closed channel flows (del Álamo & Jiménez 2006; Cossu *et al.* 2009). Figure 4 further compares G_{max} in different cases and the relative increase rate of G_{max} in the cases with deformable free surface with respect to that in the rigid-lid case for $\alpha h = 0$. As shown in figure 4(*a*), the peaks of G_{max} at different Froude numbers all occur at approximately $(\alpha h, \beta h) = (0, 2.7)$. The value of G_{max} is insensitive to the free surface when $\beta h > 2.7$. However, as the Froude number increases from $Fr_\tau = 0.05$ to $Fr_\tau = 0.142$, G_{max} increases with Fr_τ when $\beta h < 2.7$, and this growth is more obvious with lower βh (figure 4*b*).

To investigate the relationship between the free-surface effect on the transient growth and the influence of the free surface on turbulent motions that has been observed in experiments (Duan *et al.* 2020) and direct numerical simulations (Di *et al.* 2019), we analyse the effect of the free surface on the growth rate of the kinetic energy G_K corresponding to G_{max}. Here, G_K is defined based on the optimal input and output

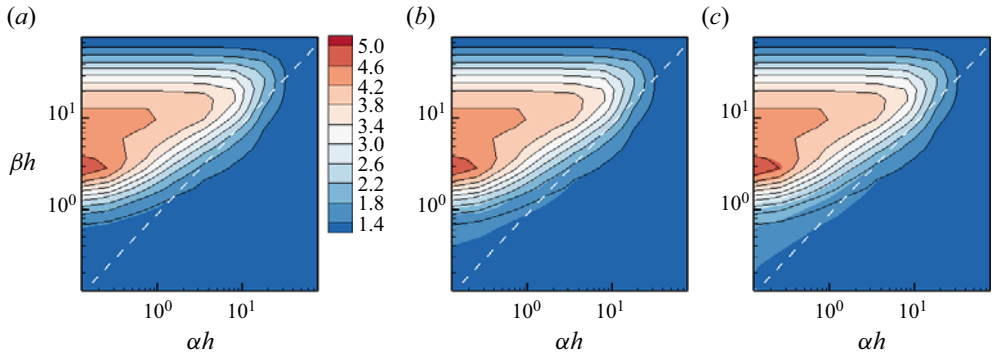

Figure 3. Comparison of the contours of the maximum transient growth rate $G_{max}(\alpha h, \beta h)$ at (*a*) $Fr_\tau = 0.05$, (*b*) $Fr_\tau = 0.1$ and (*c*) $Fr_\tau = 0.142$ with those at $Fr_\tau = 0$ for $Re_\tau = 180$. The white dashed lines represent $\alpha h = \beta h$. The solid black contours are G_{max} in the rigid-lid case ($Fr_\tau = 0$), with its value changing from 1.4 to 5 with an interval 0.4 (the same as the colour contours).

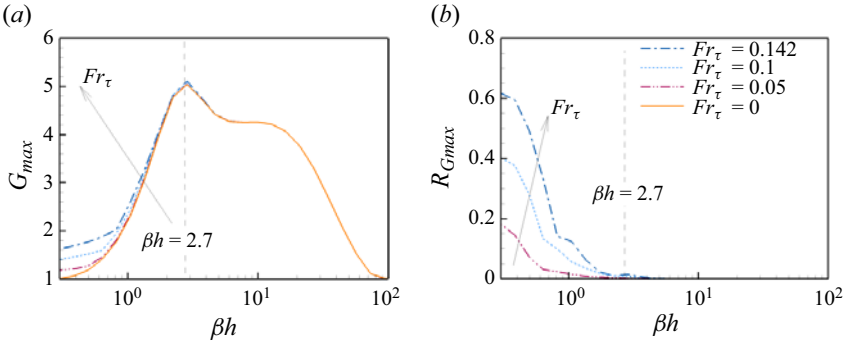

Figure 4. Comparison of (*a*) the maximum transient growth rate G_{max} at $Fr_\tau = 0$ (rigid-lid case), 0.05, 0.1 and 0.142 and (*b*) the relative increase rate, R_{Gmax}, of G_{max} in the deformable free surface cases ($Fr_\tau = 0.05$, 0.1 and 0.142) with respect to that in the rigid-lid case ($Fr_\tau = 0$). The results shown are for $\alpha h = 0$ at $Re_\tau = 180$.

perturbations corresponding to G_{max} as

$$G_K(\alpha h, \beta h, t_{max}) = \frac{E_K^{out}(\alpha h, \beta h)}{E_K^{in}(\alpha h, \beta h)} = \frac{R_K^{out} E^{out}(\alpha h, \beta h)}{R_K^{in} E^{in}(\alpha h, \beta h)} = \frac{R_K^{out}}{R_K^{in}} G_{max}(\alpha h, \beta h), \tag{3.1}$$

where R_K is the ratio of the kinetic energy to the total energy. If the ratio is larger for the amplified output perturbation than for the input perturbation, i.e. $R_K^{in} < R_K^{out} \leq 1$, $G_K > G_{max} > G_\eta$, indicating that potential energy is transformed into kinetic energy during the transient growth process. Here, G_η is the growth rate of the potential energy, which is defined as

$$G_\eta(\alpha h, \beta h, t_{max}) = \frac{E_\eta^{out}(\alpha h, \beta h)}{E_\eta^{in}(\alpha h, \beta h)} = \frac{R_\eta^{out}}{R_\eta^{in}} G_{max}(\alpha h, \beta h), \tag{3.2}$$

where R_η is the ratio of the potential energy to the total energy. If $R_K^{out} < R_K^{in} \leq 1$, kinetic energy is transformed into potential energy during the transient growth process, leading to $G_\eta > G_{max} > G_K$.

Figure 5 shows a comparison of G_{max}, G_K and G_K/G_{max} at different Froude numbers and $Re_\tau = 180$. At $Fr_\tau = 0$, the distribution of G_K is the same as that of G_{max} due to

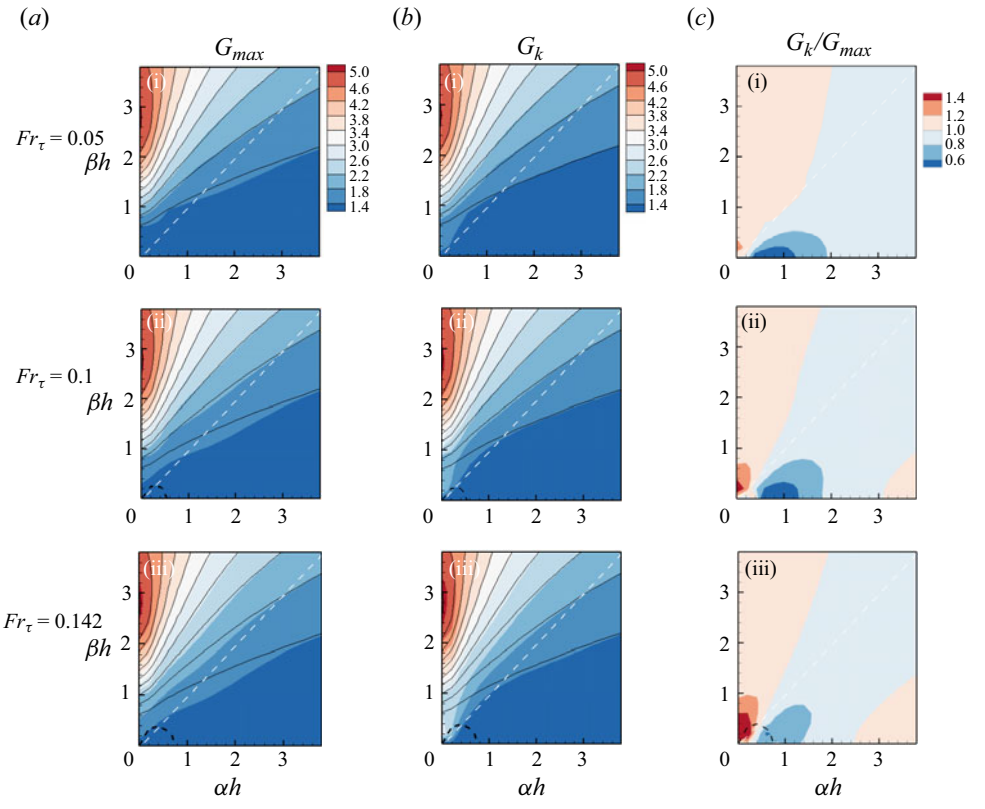

Figure 5. Comparison of (*a* i–iii) the maximum transient growth rate $G_{max}(\alpha h, \beta h)$, (*b* i–iii) the corresponding growth rate of the kinetic energy $G_K(\alpha h, \beta h)$ and (*c* i–iii) the ratio $G_K(\alpha h, \beta h)/G_{max}(\alpha h, \beta h)$ at Froude numbers $Fr_\tau =$ (*a* i,*b* i,*c* i) 0.05, (*a* ii,*b* ii,*c* ii) 0.1 and (*a* iii,*b* iii,*c* iii) 0.142 with the rigid-lid case ($Fr_\tau = 0$) at $Re_\tau = 180$. The black solid contour lines are the results in the rigid-lid case, with its value changing from 1.4 to 5 with an interval 0.4 (the same as the colour contours). The black dashed contour lines represent the locations where the imaginary part of the eigenvalue $\lambda_i = 0$. The white dashed lines represent $\alpha h = \beta h$.

the zero η. As the Froude number increases, G_K differs from G_{max}. For $\alpha h < \beta h < 2.7$, where G_{max} is enhanced by the free surface, G_K/G_{max} is close to or even larger than 1. Especially, G_K/G_{max} is obviously larger than 1 when $\alpha h < \beta h < 1$, with its largest value located at $\alpha h = 0$ (figure 5*c* iii). Therefore, when $\alpha h < \beta h < 2.7$, the growth rate of the kinetic energy also increases with increasing Froude number, with G_K being obviously greater than G_{max} for $\alpha h < \beta h < 1$.

The effect of the free surface on G_K found at $Re_\tau = 180$ also exists at $Re_\tau = 360$, 1000 and 6000. Figure 6 compares G_K at different Froude numbers for $\alpha h = 0$ when $Re_\tau = 180$, 360, 1000 and 6000. There are two peaks in G_K at different Reynolds numbers. The wavenumber of one peak is well scaled by the viscous length at approximately $\beta \nu/u_\tau = 0.07$, corresponding to the spanwise spacing of near-wall streaks. The other peak lies at approximately $\beta h = 2.4$, which agrees with the spanwise length scale of VLSMs $\lambda_z/h = 1 - 3$ in plane open channel flows (Wang & Richter 2019; Pinelli *et al.* 2022). It should be noted that these two peaks of G_K at $Re_\tau = 180$ are close to each other with comparable values, and the two peaks are more widely separated as the Reynolds number increases from $Re_\tau = 360$ to 6000. While VLSMs were not observed at Reynolds numbers lower than 442 in the experiments of open channel flows with sidewalls (Shen *et al.*

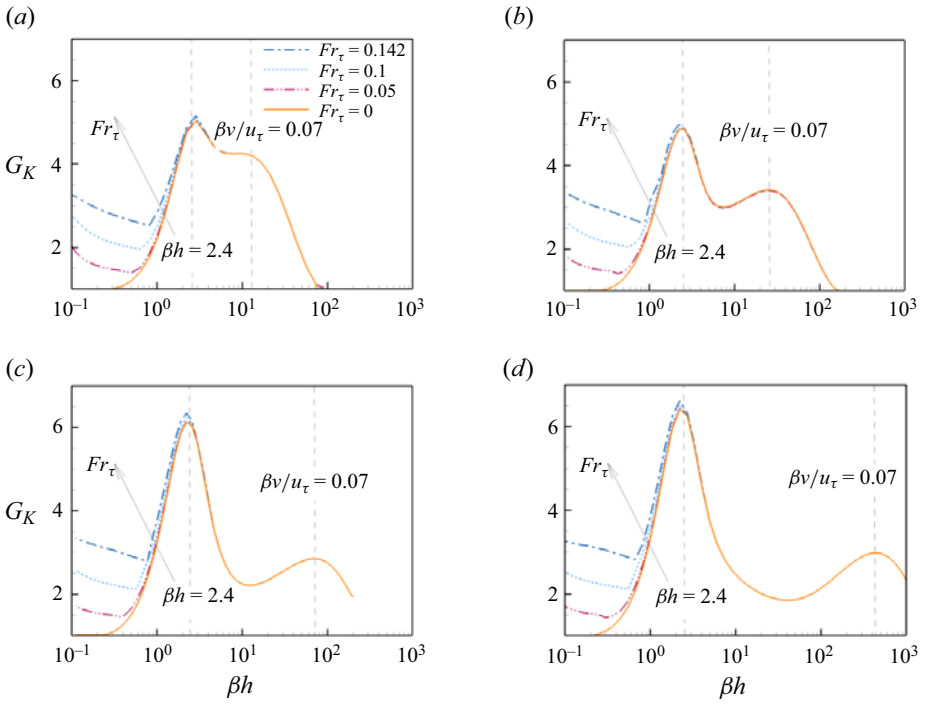

Figure 6. Influence of the Froude number on the growth rate of the kinetic energy $G_K(\alpha h, \beta h)$ corresponding to G_{max} for $\alpha h = 0$ at (*a*) $Re_\tau = 180$, (*b*) 360, (*c*) 1000 and (*d*) 6000. The first peaks are located at approximately $\beta h = 2.4$ (corresponding to $\lambda_z/h = 2.6$), and the secondary peaks are located at approximately $\beta v/u_\tau = 0.07$ (corresponding to $\lambda_z^+ = 90$).

2023), recent direct numerical simulations of plane open channel flows (Pinelli *et al.* 2022) showed that the bimodal distribution of the pre-multiplied streamwise energy spectrum of the streamwise velocity fluctuations in the outer layer is clear at $Re_\tau \geq 365$, and the peak at the length scale of VLSMs becomes weaker at a lower Reynolds number $Re_\tau = 200$. As such, the variation of the peak located around $\lambda_z/h = 2.4$ with the Reynolds number in figure 6 is similar to VLSMs in plane open channel flows.

As shown in figure 6, at these four Reynolds numbers, G_K grows with the Froude number for $\beta h \leq 2.4$, and the enhancement is more pronounced as βh decreases. From figure 7, it can be further confirmed that the enhancement of G_K by the free surface occurs for $\alpha h < \beta h$, i.e. the streamwise-elongated motions, at $Re_\tau = 360$, 1000 and 6000. Although the value of G_K (G_{max} for the rigid-lid case) around the peak located at approximately $\beta h = 2.4$ also slightly increases with the Reynolds number, similar to the finding that the intensity of VLSMs grows with the Reynolds number (Marusic *et al.* 2010; Pinelli *et al.* 2022; Pirozzoli 2023), the Froude number effect is distinct at even smaller wavenumbers. For a specified Reynolds number, the effect of free surfaces deserves attention. The above analysis suggests that the free-surface effect on the transient growth rate is consistent at least for $180 \leq Re_\tau \leq 6000$ studied in this work, and the length scale range where the free-surface effect is felt aligns with the length scale of the streamwise-elongated VLSMs that are intensified at relatively high Froude numbers in free-surface open channel flows (Di *et al.* 2019; Duan *et al.* 2020).

It should also be noted that the spanwise length scale of the peak, well scaled by h, in open channel flows is different from that in closed channel flows (Pujals *et al.* 2009). This

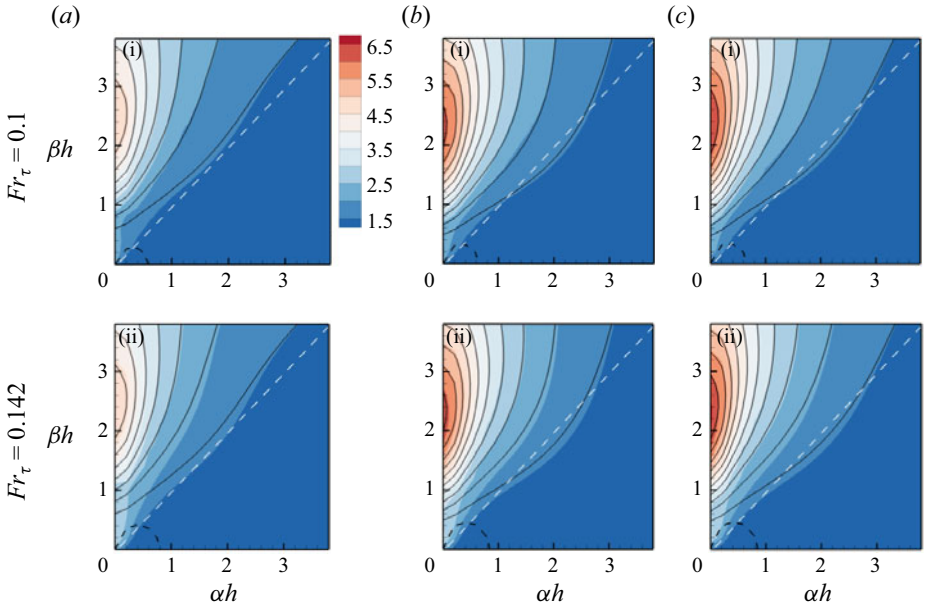

Figure 7. Comparison of the growth rate of the kinetic energy $G_K(\alpha h, \beta h)$ corresponding to the maximum transient growth rate $G_{max}(\alpha h, \beta h)$ among different Froude numbers and Reynolds numbers. Panels (*a* i,*b* i,*c* i) and (*a* ii,*b* ii,*c* ii) show the results for $Fr_\tau = 0.1$ and 0.142, respectively, while panels (*a* i,ii), (*b* i,ii) and (*c* i,ii) show the results for $Re_\tau = 360$, 1000 and 6000, respectively. Here, the black solid contour lines are the results at $Fr_\tau = 0$, with its value changing from 1.5 to 6.5 with an interval of 0.5 (the same as the colour contours). The black dashed contour lines denote the locations for which the imaginary part of the eigenvalue is zero. The white dashed lines represent $\alpha h = \beta h$.

discrepancy can be attributed to the differences in the symmetry of the mean flow and the boundary conditions. In closed channel flows, the mean velocity and boundary conditions are symmetric with respect to the channel centreline $y = h$, and hence there are two types of perturbations: one with symmetric vertical velocity and the other with asymmetric vertical velocity (Jimenez 2018). The perturbation leading to the peak in closed channel flows is a pair of streamwise vortices occupying the entire channel with symmetric vertical velocity (Pujals *et al.* 2009). However, due to the constraint imposed by the free surface, only the perturbation with asymmetric vertical velocity exists in rigid-lid open channel flows.

3.2. *Unstable eigenmodes induced by the free surface*

In addition to the influence of free surfaces on the transient growth of streamwise-elongated motions, as shown in figures 5(*a* ii,*a* iii) and 7, the free surface also induces unstable eigenmodes for spanwise-elongated motions ($\alpha h > \beta h$). In this section, we discuss these unstable eignmodes.

Figure 8(*a*,*c*) compares the eigenvalues in the free-surface open channel at $Fr_\tau = 0.142$ with those in the rigid-lid case at $Re_\tau = 180$ and 6000, with $\alpha h = 0.4$ and $\beta h = 0$. There are two additional eigenvalues in the free-surface open channel case compared with the rigid-lid case. These two additional eigenvalues and the corresponding eigenmodes, induced by the free surface, are referred to as the 'surface-wave eigenvalues' and 'surface-wave eigenmodes', respectively, while the other eigenvalues and eigenmodes

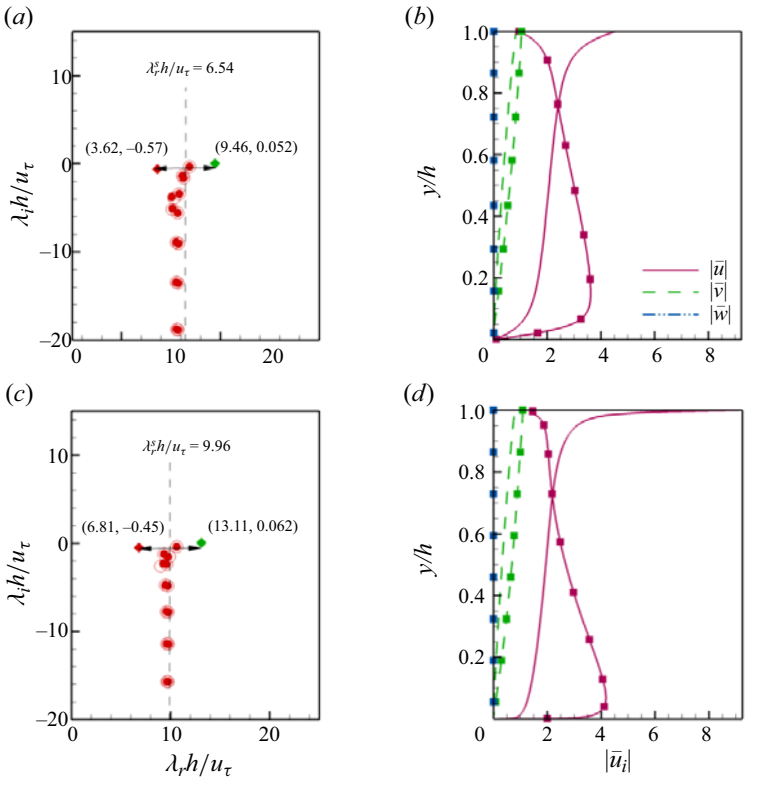

Figure 8. (*a*,*c*) Comparison of eigenvalues λ between the free-surface open channel with $Fr_\tau = 0.142$ and the rigid-lid open channel. The points represent the eigenvalues of the shear eigenmodes in the free-surface open channel, the diamonds represent the eigenvalues of the surface-wave eigenmodes in the free-surface open channel and the hollow circles represent the eigenvalues in the rigid-lid open channel. (*b*,*d*) Vertical profiles of the velocity moduli of the surface-wave eigenmodes. The lines without symbols denote the results of the unstable surface-wave eigenmode and those with symbols denote the stable surface-wave eigenmode. The results are obtained at (*a*,*b*) $Re_\tau = 180$ and (*c*,*d*) 6000 for $\alpha h = 0.4$ and $\beta h = 0$.

are called the 'shear eigenvalues' and 'shear eigenmodes', respectively (Yih 1972). In figure 8(*b*,*d*), the modulus of the vertical velocity $|\bar{v}|$ increases monotonically with y/h, reaching its maximum value at the surface and inducing surface deformation, which is another distinct feature of surface-wave eigenmodes compared with shear eigenmodes (Yih 1972).

As shown in figure 8(*a*,*c*), the propagation speeds $c = \lambda_r/\alpha$ of these two surface-wave eigenmodes are different. Assume that these two speeds are $c_1 = c_s + c_w$ and $c_2 = c_s - c_w$. It can be found that the values of c_s (equal to λ_r^s/α) at $Re_\tau = 180$ and 6000 are approximately $16.3u_\tau$ and $25u_\tau$, respectively, close to the mean velocity near the surface. The value of c_w/u_τ is close to the phase speed determined by the dispersion relationship $\sqrt{\tanh(kh)}/(Fr_\tau\sqrt{kh})$. The unstable eigenmode is the surface-wave eigenmode with $c_1 = c_s + c_w$.

In the stability analysis using the laminar base flow, the unstable surface-wave eigenmode also has been found at small αh. For the horizontal plane open channel flow, the condition leading to the unstable eigenmodes is $Fr_b > 0.8$ (Olsson & Henningson 1995). In the present work, the unstable eigenmodes exist in supercritical cases. Because the mean velocity profile used in this study is complex, it is difficult to provide an exact

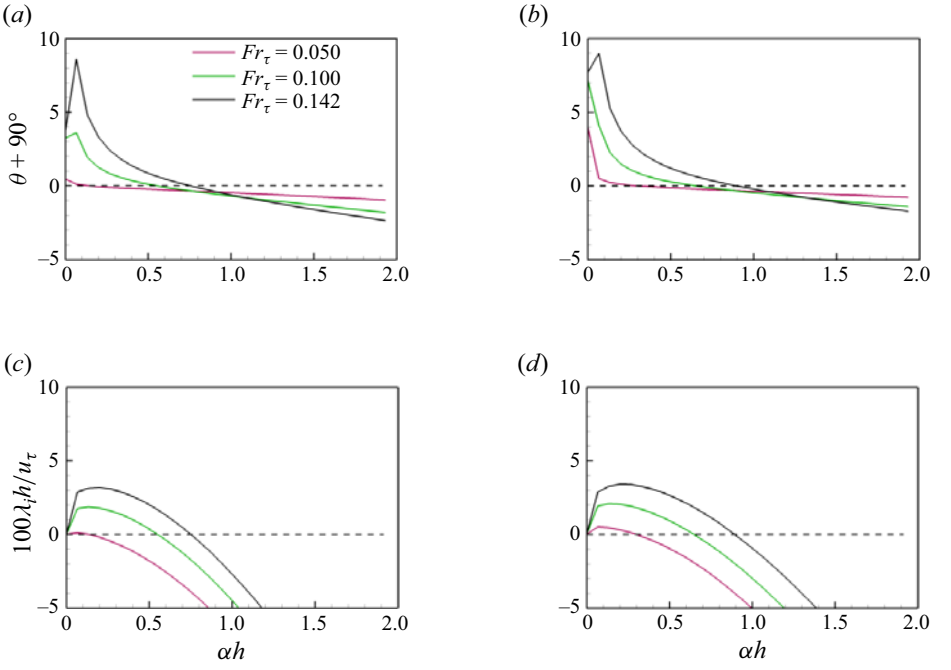

Figure 9. Variations of the phase difference between the vertical velocity and the surface elevation θ and the corresponding eigenvalue λ_i with αh at $\beta h = 0$ for the surface-wave eigenmodes with $c_1 = c_s + c_w$. (*a*) $\theta + 90°$ at $Re_\tau = 180$, (*b*) $\theta + 90°$ at $Re_\tau = 6000$, (*c*) $100\lambda_i h/u_\tau$ at $Re_\tau = 180$, (*d*) $100\lambda_i h/u_\tau$ at $Re_\tau = 6000$.

formulation to determine the lowest unstable Froude numbers. We provide another feature based on the boundary condition. From (2.15), it can be derived that

$$\hat{\eta} = \frac{\hat{v}}{-\mathrm{i}\lambda_r + \mathrm{i}\alpha U_s + \lambda_i} = \frac{\hat{v}}{|\mathrm{i}(\alpha U_s - \lambda_r) + \lambda_i|}\exp(\mathrm{i}\theta), \quad \text{with } \tan\theta = \frac{\lambda_r - \alpha U_s}{\lambda_i}. \tag{3.3}$$

Here, U_s is the mean velocity at the free surface. For the free-surface eigenmode with $c_1 = c_s + c_w$, the flow is neutrally stable ($\lambda_i = 0$) when $\theta = -90°$, and becomes unstable when $\theta > -90°$. This is confirmed by figure 9, which shows that the range of βh where $\theta + 90° > 0$ (figure 9*a*,*c*) agrees with that with $\lambda_i > 0$ (figure 9*b*,*d*) for different Reynolds numbers and Froude numbers. From figure 9, the streamwise length of these unstable eigenmodes is longer than $2\pi h$, i.e. $\alpha h < 1$. These unstable modes are much longer than those obtained in the secondary stability analysis of open channel flows with secondary currents (close to $3h$) (Camporeale *et al.* 2021).

As these unstable eigenmodes are surface waves with $\beta h < \alpha h$, their exponential growth is not directly responsible for the enhancement of streamwise-elongated VLSMs found in free-surface open-channel flows (Di *et al.* 2019; Duan *et al.* 2020). It is known that surface waves can enhance VLSMs through the nonlinear Craik–Leibovich mechanism (Craik & Leibovich 1976) when the surface waves are strong enough. However, the exponential growth rates of these unstable eigenmodes are small. For example, the imaginary part of the eigenvalue for the most unstable eigenmode is $\lambda_i h/u_\tau \approx 0.07$ at $Fr_\tau = 0.142$ and $Re_\tau = 6000$, and the corresponding exponential growth rate of the perturbation energy $\exp(2\lambda_i t)$ is equal to $\exp(0.14tu_\tau/h)$. The maximum value of t_{max}, the time when the maximum transient growth is reached, slightly increases with the Reynolds number

from $1.8h/u_\tau$ at $Re_\tau = 180$ to $2.4h/u_\tau$ at $Re_\tau = 6000$ (see Appendix A), comparable with the time required for the growth of very-large-scale streaks (Hwang & Bengana 2016). During the time scale of the growth of very-large-scale streaks, the exponential growth rate of the unstable surface wave is less than 1.25. In fact, the features of Langmuir-type flow driven by the nonlinear Craik–Leibovich mechanism, such as the disrupted logarithmic layer (Deng *et al.* 2019; Peruzzi *et al.* 2021), have not been reported in free-surface open-channel flows without externally generated waves. Therefore, these unstable surface-wave eigenmodes cannot grow sufficiently to influence VLSMs through the nonlinear Craik–Leibovich mechanism.

The above analyses suggest that compared with the linear instability induced by the free surface, the effect of the free surface on non-modal transient growth is more closely associated with the amplification of VLSMs by the free surface. This result is consistent with the findings in other canonical wall-bounded turbulence, that the non-modal transient growth is crucial for the generation of very-large-scale streaks (Hwang & Bengana 2016; Cossu & Hwang 2017). The mechanism of free surfaces influencing the transient growth rate is analysed in detail in § 4 below.

4. Effects of the free surface on streamwise-elongated motions

In this section, we investigate the mechanisms by which the free surface affects the transient growth of streamwise-elongated ($\alpha h \ll \beta h$) motions. The mechanism for streamwise-uniform ($\alpha h = 0$) motions is first investigated in § 4.1, and the effects of the Froude number Fr_τ and the spanwise wavenumber βh at different Reynolds numbers are examined. Then, in § 4.2, the mechanism is extended to streamwise-varying motions to show the influence of the streamwise wavenumber αh.

4.1. *Streamwise-uniform motions*

In this section, we conduct transient growth analyses of motions that are uniform in the streamwise direction, i.e. $\alpha h = 0$. The case with $Re_\tau = 180$, $Fr_\tau = 0.142$, $\alpha h = 0$ and $\beta h = 1$ is used as an example to illustrate the results. We first show the influence of the free surface on the eigenvalues, eigenmodes and energy growth rate. The budget equation of the perturbation energy is analysed to elucidate the dynamic mechanism underlying how the free surface influences the energy growth rate. Then, we derive the initial conditions of the flow field and the free-surface elevation that enhance the energy transient growth rate. Finally, the mechanism is used to explain the variation in the free-surface effect on the energy transient growth rate with the Froude number and the spanwise wavenumber at different Reynolds numbers.

4.1.1. *Surface-wave eigenmodes and their impacts on energy growth*

Figure 10(*a*) shows the eigenvalues in the free-surface open channel at $Re_\tau = 180$, $Fr_\tau = 0.142$, $\alpha h = 0$ and $\beta h = 1$. The eigenvalues in the corresponding rigid-lid open channel at the same wavenumber and Reynolds number are also plotted in figure 10(*a*) for comparison. There are two additional eigenvalues in the free-surface open channel case compared with the rigid-lid open channel case. These two additional eigenvalues and the corresponding eigenmodes induced by the free surface are referred to as the 'surface-wave eigenvalues' and 'surface-wave eigenmodes', respectively, while the other eigenvalues and eigenmodes are called the 'shear eigenvalues' and 'shear eigenmodes', respectively (Yih 1972). In contrast to the zero values of the real parts of the eigenvalues of the shear

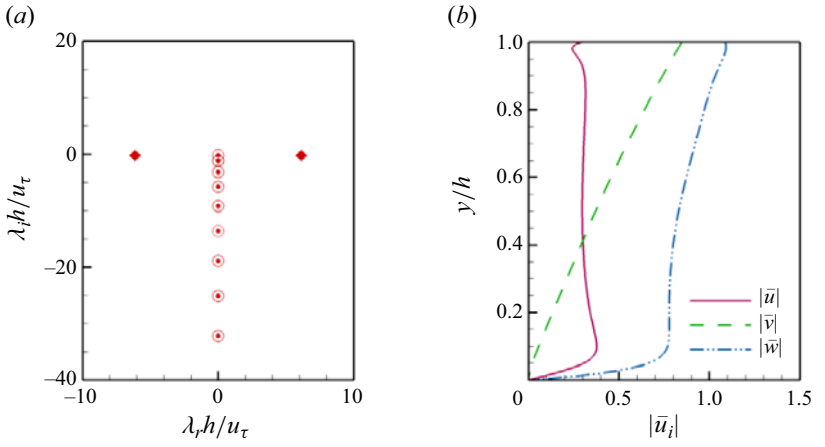

Figure 10. (*a*) Comparison of eigenvalues λ between the free-surface open channel with $Fr_\tau = 0.142$ and the rigid-lid open channel. The points represent the eigenvalues of the shear eigenmodes in the free-surface open channel, the diamonds represent the eigenvalues of the surface-wave eigenmodes in the free-surface open channel and the hollow circles represent the eigenvalues in the rigid-lid open channel. (*b*) Vertical profiles of the velocity moduli of the surface-wave eigenmodes. The results are obtained at $Re_\tau = 180$, $\alpha h = 0$ and $\beta h = 1$.

eigenmodes, $\lambda_r = 0$, the two surface-wave eigenmodes have the same imaginary parts λ_i but opposite non-zero real parts λ_r, indicating that the two surface-wave eigenmodes propagate in opposite spanwise directions with identical phase speeds $|\lambda_r/\beta|$ and the same damping rate λ_i. Here, $|\lambda_r|$ represents the frequency of the surface-wave eigenmodes. The velocity moduli of the two surface-wave eigenmodes have the same vertical profiles. Figure 10(*b*) shows the profiles of the velocity moduli $|\bar{u}|$, $|\bar{v}|$ and $|\bar{w}|$ of the surface-wave eigenmodes. The streamwise velocity modulus $|\bar{u}|$ is non-zero due to the presence of the non-uniform base flow $U(y)$, and a viscous Stokes layer appears in the profiles of $|\bar{u}|$ and $|\bar{w}|$ near the bottom. The modulus of the vertical velocity $|\bar{v}|$ increases monotonically with y, reaching its maximum value at the surface and inducing surface deformation, which is another distinct feature of surface-wave eigenmodes compared with shear eigenmodes (Yih 1972).

The surface-wave eigenmodes induced by the free surface have significant effects on the transient growth of the total energy E and kinetic energy E_K. Figure 11 shows the evolution of $E(t)/E^{in}$ and $E_K(t)/E_K^{in}$ with time. The results are compared among the rigid-lid open channel, free-surface open channel ($Fr_\tau = 0.142$) with surface-wave eigenmodes, and free-surface open channel ($Fr_\tau = 0.142$) without surface-wave eigenmodes at $Re_\tau = 180$, $\alpha h = 0$ and $\beta h = 1$. In each case, the initial input perturbations are those that lead to the homologous maximum transient growth rates. As shown in figure 11(*a*), in the rigid-lid case, $E(t)/E^{in}$ initially increases monotonically with time due to the non-orthogonality of the eigenmodes; then the maximum value G_{max} is reached at $tu_\tau/h \approx 1.5$; and finally, $E(t)/E^{in}$ decreases because the eigenmodes are stable. For the free-surface open channel case, when the surface-wave eigenmodes are excluded, $E(t)/E^{in}$ is the same as in the rigid-lid case, indicating that the surface elevation induced by the shear eigenmodes is negligible. In contrast, when the surface-wave eigenmodes are considered, $E(t)/E^{in}$ increases with oscillations for $0 < tu_\tau/h < 1.5$. The oscillation period is close to the period of the surface-wave eigenmodes $T = 2\pi h/(|\lambda_r|u_\tau) = 1.05h/u_\tau$ (see $|\lambda_r|$ in figure 10*a*). Accompanied by the oscillation, $E(t)/E^{in}$ is larger in the free-surface open channel case with surface-wave eigenmodes than in the other two cases for most

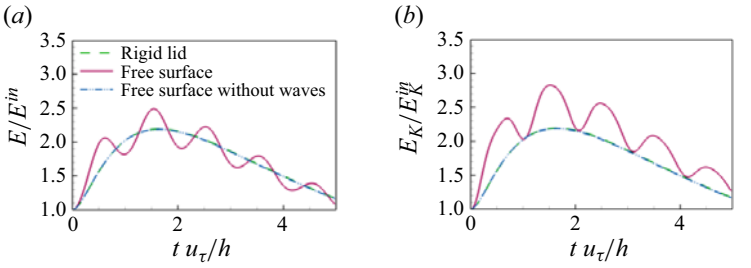

Figure 11. Comparisons of (*a*) $E(t)/E^{in}$ and (*b*) $E_K(t)/E_K^{in}$ among the rigid-lid open channel flow, free-surface open channel flow ($Fr_\tau = 0.142$) with surface-wave eigenmodes and free-surface open channel flow ($Fr_\tau = 0.142$) without surface-wave eigenmodes. Note that the curves in the first case and the third case overlap. The results are obtained at $Re_\tau = 180$, $\alpha h = 0$ and $\beta h = 1$, with the initial perturbations leading to G_{max}.

of the duration $0 < tu_\tau/h < 1.5$. The above comparison of $E(t)/E^{in}$ among the three cases indicates that the surface-wave eigenmodes are responsible for the larger G_{max} in the free-surface open channel than in the rigid-lid open channel.

The temporal development of the kinetic energy $E_K(t)/E_K^{in}$ is also considerably influenced by the surface-wave eigenmodes. As shown in figure 11(*b*), when the surface-wave eigenmodes are excluded, $E_K(t)/E_K^{in}$ in the free-surface open channel is equal to $E_K(t)/E_K^{in}$ (which is equal to $E(t)/E^{in}$) in the rigid-lid open channel (figure 11*a*). However, when the surface-wave eigenmodes in the free-surface open channel are included, $E_K(t)/E_K^{in}$ oscillates with a value larger than $E(t)/E^{in}$ shown in figure 11(*a*). The maximum value of $E_K(t)/E_K^{in}$ in the free-surface open channel case is approximately 27 % larger than that in the rigid-lid open channel case. Similar to the analyses of G_K (figure 5) based on the relationship in (3.1), the ratio of the kinetic energy to the total energy satisfies $R_K^{in} < R_K(t) \leq 1$, implying that the larger value of $E_K(t)/E_K^{in}$ than $E(t)/E^{in}$ is correlated with the initial potential energy induced by the surface-wave eigenmodes. This result is confirmed by the analyses in the next section.

4.1.2. *Impact of surface-wave eigenmodes on the energy budget*

Next, the governing equations of the total perturbation energy and kinetic energy are derived and analysed to elucidate how the surface-wave eigenmodes affect the maximum transient growth rate. By applying the dot product of $\boldsymbol{u}$ on both sides of (2.2), integrating over the whole open channel and over time, and replacing the surface pressure with the surface boundary condition (2.7), we derive that

$$\frac{E(t)}{E^{in}} = 1 + \frac{P(t)}{E^{in}} + \frac{S(t)}{E^{in}} + \frac{V(t)}{E^{in}} + \frac{\epsilon(t)}{E^{in}}. \tag{4.1}$$

In (4.1), P, S, V and ϵ refer to the integrals of the energy production term, the surface energy transfer term, the non-constant eddy viscosity term and the viscous dissipation term, respectively. They are defined as

$$P(t) = -\int_0^t \int_0^h \overline{uv} U' \,\mathrm{d}y\,\mathrm{d}t, \tag{4.2}$$

$$S(t) = \int_0^t \left[-\nu \frac{\partial \overline{vv}}{\partial y} + \frac{1}{2}\nu_T \frac{\partial \overline{u_i u_i}}{\partial y} \right]_{y=h} \mathrm{d}t, \tag{4.3}$$

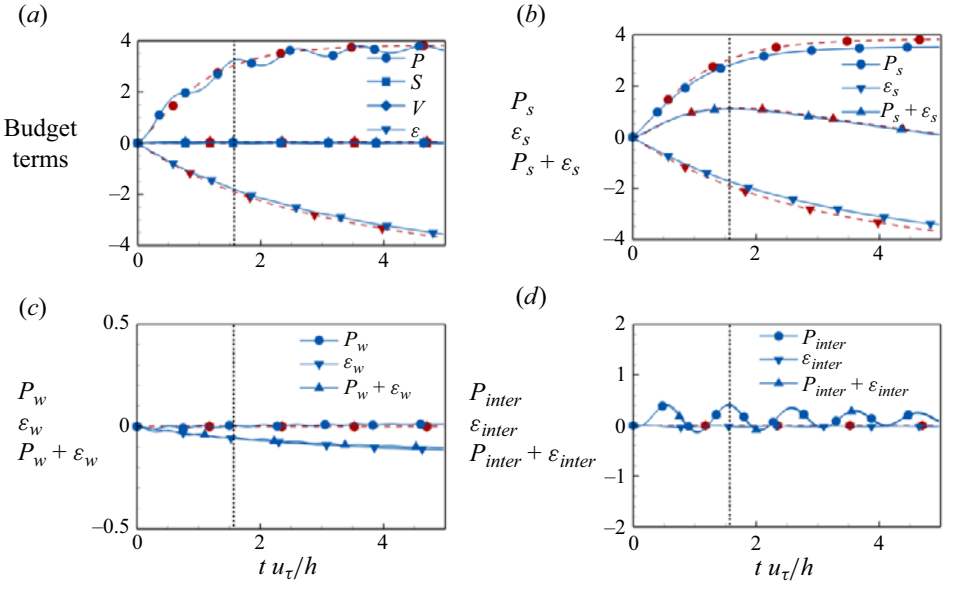

Figure 12. Time evolution of the budget terms (4.1) and their components (4.7) and (4.9) normalised by E^{in} in the rigid-lid open channel (red dashed lines with symbols) and free-surface open channel (black solid lines with symbols) cases. The results are obtained at $Re_\tau = 180$, $\alpha h = 0$ and $\beta h = 1$, with the initial input perturbations leading to G_{max}. For the free-surface open channel, $Fr_\tau = 0.142$.

$$V(t) = \int_0^t \int_0^h \frac{\partial \nu_T}{\partial y} \left(\frac{\partial \overline{v}\,\overline{v}}{\partial y} + \frac{1}{2} \frac{\partial \overline{u_i} \overline{u_i}}{\partial y} \right) \mathrm{d}y\,\mathrm{d}t, \tag{4.4}$$

$$\epsilon(t) = -\int_0^t \int_0^h \nu_T \overline{\frac{\partial u_i}{\partial x_j} \frac{\partial u_i}{\partial x_j}}\,\mathrm{d}y\,\mathrm{d}t. \tag{4.5}$$

The overline denotes averaging over the horizontal plane. The term S is zero in the rigid-lid open channel flow. For a given wavenumber, $(u_i, \eta) = (\hat{u}_i, \hat{\eta}) \exp(\mathrm{i}(\alpha x + \beta z - \lambda t)) + \mathrm{c.c.}$

Figure 12(*a*) shows the time evolution of the budget terms normalised by E^{in} in (4.1) at $Re_\tau = 180, \alpha h = 0, \beta h = 1$ and $Fr_\tau = 0.142$. The vertical dashed line indicates the time at which the maximum transient growth rate is reached. In contrast to common expectations, the contribution of the surface transfer term S to the total energy growth is negligible in the free-surface open channel case, although the surface is deformable. The non-uniform eddy viscosity term V is also negligible in both the rigid-lid and free-surface open channel cases, because it works as a turbulent diffusion term in the transport of turbulent kinetic energy. Therefore, the transient growth rates in the two cases are governed by the net effect of the other two terms, the production term P and the dissipation term ϵ.

The effect of the free surface on the balance between the energy production term P and the dissipation term ϵ is investigated next. Assume that the perturbation consists of a surface-wave part and a shear part, i.e.

$$(u_i, \eta) = (u_{iw} + u_{is}, \eta_w + \eta_s). \tag{4.6}$$

The subscript 'w' denotes the surface-wave part, which is a linear combination of the surface-wave eigenmodes, and the subscript 's' refers to the shear part, which is a linear combination of the shear eigenmodes. Correspondingly, P and ϵ can also be decomposed

into a surface-wave part, a shear part and an interaction part, i.e.

$$P = -\int_0^t \int_0^h \left(\overline{u_w v_w} + \overline{u_s v_s} + \overline{u_s v_w + u_w v_s}\right) U' \,\mathrm{d}y \,\mathrm{d}t = P_w + P_s + P_{inter}, \tag{4.7}$$

and

$$\epsilon = -\int_0^t \int_0^h \nu_T \left(\overline{\frac{\partial u_{iw}}{\partial x_j}\frac{\partial u_{iw}}{\partial x_j}} + \overline{\frac{\partial u_{is}}{\partial x_j}\frac{\partial u_{is}}{\partial x_j}} + \overline{\frac{\partial u_{iw}}{\partial x_j}\frac{\partial u_{is}}{\partial x_j}} + \overline{\frac{\partial u_{is}}{\partial x_j}\frac{\partial u_{iw}}{\partial x_j}} \right) \mathrm{d}y \,\mathrm{d}t \tag{4.8}$$

$$= \epsilon_w + \epsilon_s + \epsilon_{inter}. \tag{4.9}$$

The interaction parts, denoted by the subscript 'inter', exist because the eigenmodes are non-normal. For the rigid-lid case, the surface-wave part and the interaction part do not exist, and thus, $P = P_s$ and $\epsilon = \epsilon_s$.

For the shear part, figure 12(b) shows that the magnitudes of P_s and ϵ_s normalised by E^{in} are slightly smaller in the free-surface open channel than in the rigid-lid open channel, and $P_s + \epsilon_s$ is comparable between these two cases. Therefore, the free surface has an insignificant effect on the contribution of the shear part to the energy growth rate $E(t)/E^{in}$.

For the surface-wave part, as illustrated in figure 12(c), the surface wave gains little energy from the base flow because the surface-wave part of the energy production term P_w is nearly zero. The dissipation ϵ_w is negative, consistent with the negative imaginary parts of the eigenvalues λ_i in figure 10(a). Consequently, the combined surface-wave part $P_w + \epsilon_w$ has a negative contribution to the energy growth rate $E(t)/E^{in}$. However, when the surface-wave part is present, figure 12(d) shows that the net contribution of the interaction between the surface-wave part and the shear part, $P_{inter} + \epsilon_{inter}$, oscillates with mainly positive values, and the magnitude of this term is greater than $P_w + \epsilon_w$. Therefore, the presence of the surface-wave part increases the energy growth rate $E(t)/E^{in}$ through the interaction part.

Due to the small magnitude of ϵ_{inter}, the quasi-positive contribution of the interaction part to $E(t)/E^{in}$ occurs due to P_{inter} (figure 12d). The interaction production term P_{inter} can be decomposed as follows:

$$P_{inter} = P_{inter1} + P_{inter2} = -\int_0^t \overline{u_s v_w} U' \,\mathrm{d}y \,\mathrm{d}t - \int_0^t \overline{u_w v_s} U' \,\mathrm{d}y \,\mathrm{d}t. \tag{4.10}$$

As shown in figure 13, P_{inter} is dominated by P_{inter1}, i.e.

$$P_{inter} \approx P_{inter1} = -\int_0^t \overline{u_s v_w} U' \,\mathrm{d}y \,\mathrm{d}t. \tag{4.11}$$

This is because among the four velocity components in (4.10), only u_s increases with time (shown below). In conclusion, the free surface leads to the amplification and oscillation of $E(t)/E^{in}$ due to the energy production, which is related to the interaction between the vertical velocity of the surface-wave part v_w and the streamwise velocity of the shear part u_s. The effect of the interaction production term is also confirmed at $Re_\tau = 6000$ in Appendix B.

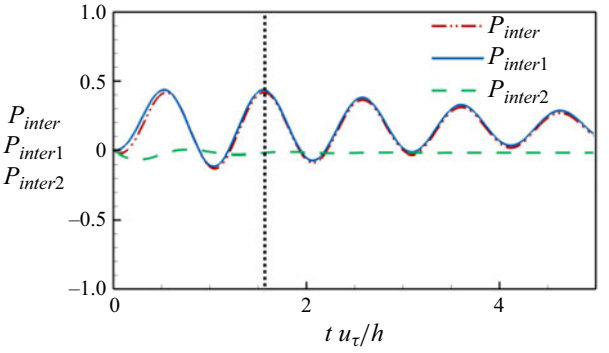

Figure 13. Decomposition of P_{inter} (4.10) obtained at $Re_\tau = 180$, $Fr_\tau = 0.142$, $\alpha h = 0$ and $\beta h = 1$.

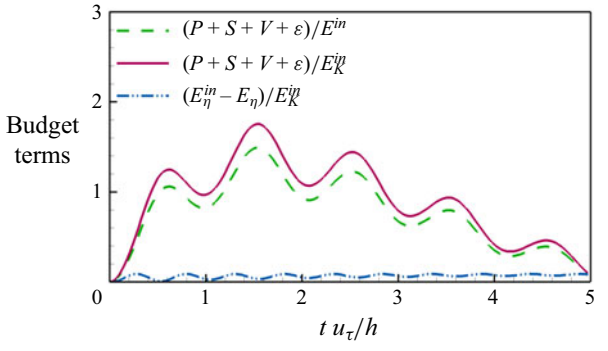

Figure 14. Time evolution of the budget terms in (4.12). The results are obtained in a free-surface open channel at $Re_\tau = 180$, $\alpha h = 0$, $\beta h = 1$ and $Fr_\tau = 0.142$.

The governing equation of the kinetic energy $E_K(t)/E_K^{in}$ can be derived from (4.1) as

$$\frac{E_K(t)}{E_K^{in}} = 1 + \frac{P+S+V+\epsilon}{E_K^{in}} + \frac{E_\eta^{in} - E_\eta(t)}{E_K^{in}}. \tag{4.12}$$

The second term on the right-hand side of (4.12),

$$\frac{P+S+V+\epsilon}{E_K^{in}} = \frac{P+S+V+\epsilon}{E^{in} R_K^{in}}, \tag{4.13}$$

represents the net contribution of the energy production, surface energy transfer, and the effects of non-uniform eddy viscosity and dissipation. The third term, $(E_\eta^{in} - E_\eta(t))/E_K^{in}$, represents the transformation of potential energy to kinetic energy. Figure 14 shows the time evolution of the budget terms in (4.12), with the term $(P+S+V+\epsilon)/E^{in}$ included for comparison. The results demonstrate that $(P+S+V+\epsilon)/E_K^{in}$ is larger than $(P+S+V+\epsilon)/E^{in}$, indicating the large initial potential energy E_η^{in}. In addition, $(E_\eta^{in} - E_\eta(t))/E_K^{in}$ is positive and oscillates at a period equal to half of the period of the surface-wave eigenmodes $T = 1.05h/u_\tau$, suggesting that the initial potential energy is associated with the surface-wave part.

The above analyses of the energy budget equation show that the initial surface-wave part contains considerable potential energy E_η^{in} and interacts with the shear part, leading to a

maximum in the quasi-positive energy production term. This in turn leads to greater values of G_{max} and G_K in the free-surface case than in the rigid-lid case, as shown in figures 3–7.

4.1.3. *Initial fields that enhance the energy growth rate of streamwise-uniform motions*

Next, we study the state of the initial flow, especially the phase relationship between the surface-wave part and the shear part, which can maximise the energy production term P_{inter1}/E^{in} in (4.11).

Figure 15 displays the flow fields, surface deformation, and their shear and surface-wave parts at $t = iT/4$, with $i = 0, 1, \ldots, 6$. Here, T is the period of the two surface-wave eigenmodes corresponding to the frequency $|\lambda_r|$ in figure 10(*a*), which equals $1.05h/u_\tau$. The initial flow field consists of a pair of strong streamwise vortices denoted by the vector (v, w) and relatively weak streaks of streamwise velocity u, with an apparent surface elevation η (figure 15*a* i). The initial (v, w) originates from the shear part (v_s, w_s) (figure 15*b* i), because the initial vertical and spanwise velocities contributed by the surface-wave part are approximately zero, i.e. $v_w \approx 0$ and $w_w \approx 0$ (figure 15*c* i). The initial streamwise velocity u (figure 15*a* i) is contributed by the shear part u_s (figure 15*b* i) and the relatively weak surface-wave part u_w, which have opposite signs (figure 15*c* i). The initial surface deformation η is determined by the surface-wave part η_w (figure 15*a* i,*c* i). The zero initial vertical and spanwise velocities under the obvious spanwise wave (figure 15*c* i) indicate that the surface wave is not a progressive wave but rather a standing wave composed of two surface-wave eigenmodes with the same frequency propagating in opposite directions (figure 10*a*). This finding is confirmed by the time evolution of the surface deformation of the surface-wave part (figure 15*c* i–*c* vii). The surface elevation of the initial standing wave is in phase with the streamwise velocity generated by the lifting-up of the mean shear by streamwise vortices.

Over time, the streamwise vortices (figure 15*b* i–*b* vii) in the shear part attenuate to amplify the streamwise velocity u_s, similar to the generation of streaks by the lifting-up effect in closed channel flows (Pujals *et al.* 2009). Moreover, due to the small negative value of λ_i for the two surface-wave eigenmodes (figure 10*a*), the magnitudes of the surface elevation and the velocity fields induced by the standing wave attenuate slowly and oscillate (figure 15*c* i–*c* vii), which is consistent with the oscillation of the positive $(E_\eta^{in} - E_\eta(t))/E_K^{in}$ term in figure 14. Combining the two parts, the amplified flow field at the time when G_{max} is reached is featured by strong streaks (figure 15*a* vii). Therefore, the streaks are amplified at the expense of the initial streamwise vortices and the standing wave in the free-surface open channel.

It can be proven that only the initial state of the surface-wave part shown in figure 15(*c* i) can maximise the energy production term P_{inter1}/E^{in}, which is correlated with the interaction between the surface-wave part and the shear part (4.11). For the shear part, the shear eigenmodes have λ_r values of zero (figure 10*a*), i.e. zero frequency. The distribution of the shear part in the y–z plane is similar at different times, with the magnitude varying with time (figure 15*b* i–*b* vii). In particular, the locations of the streamwise vortices and streaks do not change with time. However, the magnitudes of the streamwise vortices decrease with time, and the intensity of the streaks increases with time. Therefore, the velocities of the shear part can be assumed to be

$$u_s = f_{us}(y)g(t)\cos(\beta z + \theta_s), \tag{4.14}$$

$$v_s = -f_{vs}(y)m(t)\cos(\beta z + \theta_s), \tag{4.15}$$

$$w_s = -f_{ws}(y)n(t)\sin(\beta z + \theta_s). \tag{4.16}$$

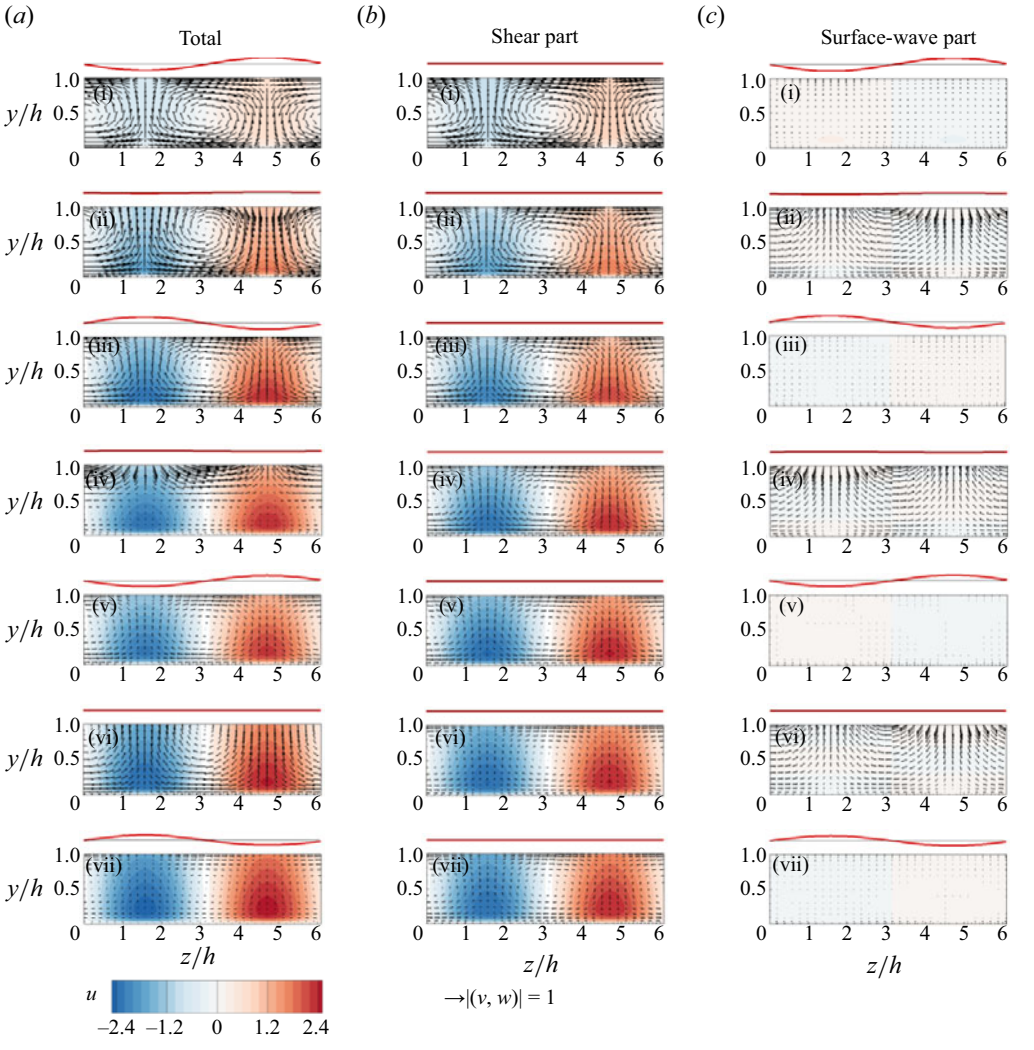

Figure 15. Velocity field and surface elevation, as well as their shear and surface-wave parts, at (*a* i–*c* i) $t = 0$, (*a* ii–*c* ii) $t = T/4$, (*a* iii–*c* iii) $t = T/2$, (*a* iv–*c* iv) $t = 3T/4$, (*a* v–*c* v) $t = T$, (*a* vi–*c* vi) $t = 5T/4$ and (*a* vii–*c* vii) $t = 3T/2$. Panels (*a* i–*a* vi) show the total, panels (*b* i–*b* vii) depict the shear part and panels (*c* i–*c* vii) display the surface-wave part. Here, T is the period of the two surface-wave eigenmodes, and the maximum transient growth is reached at $t = 3T/2$. The vector is composed of the vertical and spanwise velocities, and the contours are the streamwise velocity.

Here, f_{us} and f_{vs} are positive, and the sign of f_{ws} changes near the channel centre. The time functions satisfy $g(t) \geq 1$, $m(t) \leq 1$ and $n(t) \leq 1$, with $g(0) = m(0) = n(0) = 1$. The angle θ_s indicates the phase of the shear part in the spanwise direction.

The surface-wave part is a linear combination of the two surface-wave eigenmodes, i.e.

$$u_w = f_{uw}(y)\,[-a_1 \sin(\beta z + |\lambda_r| t + \theta_{w1}) + a_2 \sin(\beta z - |\lambda_r| t + \theta_{w2})]\,\mathrm{e}^{\lambda_i t}, \tag{4.17}$$

$$v_w = f_{vw}(y)\,[a_1 \cos(\beta z + |\lambda_r| t + \theta_{w1}) + a_2 \cos(\beta z - |\lambda_r| t + \theta_{w2})]\,\mathrm{e}^{\lambda_i t}, \tag{4.18}$$

$$w_w = f_{ww}(y)\,[-a_1 \sin(\beta z + |\lambda_r| t + \theta_{w1}) - a_2 \sin(\beta z - |\lambda_r| t + \theta_{w2})]\,\mathrm{e}^{\lambda_i t}, \tag{4.19}$$

$$\eta_w = f_\eta\,[a_1 \sin(\beta z + |\lambda_r| t + \theta_{w1}) - a_2 \sin(\beta z - |\lambda_r| t + \theta_{w2})]\,\mathrm{e}^{\lambda_i t}, \tag{4.20}$$

where $f_{uw}(y)$, $f_{vw}(y)$ and $f_{ww}(y)$ are the moduli of the surface-wave eigenmodes (figure 10*b*) and θ_{w1} and θ_{w2} are the phases of the two surface-wave eigenmodes. Note that λ_i and λ_r are the attenuation rate and frequency of the surface-wave eigenmodes, respectively (figure 10*a*), and f_η is the surface elevation in the eigenmodes. The parameters a_1 and a_2 are positive. We assume that for the surface-wave part, the small phase change in the vertical velocity of the surface-wave eigenmodes can be ignored. The phase relationships $\theta_s - \theta_{w1}$ and $\theta_s - \theta_{w2}$, and the relationship between a_1 and a_2 needed to maximise P_{inter1}/E^{in} are derived below.

Here, P_{inter1} (4.11) can be approximated as

$$P_{inter1} \approx -\frac{1}{2}F \sum_{n=0}^{N} \frac{\Phi^{(n)}(0)}{|\lambda_r| n!} t^n (a_1 \sin(|\lambda_r| t + \theta_{w1} - \theta_s) + a_2 \sin(|\lambda_r| t + \theta_s - \theta_{w2}) + \frac{a_1 F \sin(\theta_{w1} - \theta_s) + a_2 F \sin(\theta_s - \theta_{w2})}{2|\lambda_r|}, \tag{4.21}$$

with

$$F = \int_0^h f_{us}(y) f_{vw}(y) U' \,\mathrm{d}y \tag{4.22}$$

and

$$\Phi(t) = g(t)\mathrm{e}^{\lambda_i t}. \tag{4.23}$$

Here, $\Phi^{(n)}(0)$ is the nth derivative of Φ at $t = 0$. Equation (4.21) is obtained based on the Taylor expansion of Φ at $t = 0$. The first term on the right-hand side of (4.21) is responsible for the oscillation of P_{inter1}, and the second term is a constant. When $\theta_{w1} - \theta_s = \pi/2$ and $\theta_s - \theta_{w2} = \pi/2$, the second term reaches its positive maximum value, which leads to a quasi-positive P_{inter}. Under such conditions,

$$P_{inter1} = -\frac{(a_1 + a_2)F}{2} \sum_{n=0}^{N} \frac{\Phi^{(n)}(0)}{|\lambda_r| n!} t^n \sin(|\lambda_r| t + \pi/2) + \frac{(a_1 + a_2)F}{2|\lambda_r|}. \tag{4.24}$$

For specified Re_τ, Fr_τ, αh and βh, the values of F, λ_r and $\Phi^{(n)}(0)$ are constant. The maximum value of P_{inter1} increases with $a_1 + a_2$.

To obtain the maximal P_{inter}/E^{in}, the relationship between a_1 and a_2 that minimises E^{in} must be determined. Keeping the shear part constant, a_1 and a_2 should be chosen to minimise the sum of the surface-wave part of the kinetic energy $(E_K)_w^{in}$, the interaction part of the kinetic energy $(E_K)_{inter}^{in}$ and the surface-wave part of the potential energy $(E_\eta)_w^{in}$. The interaction part of the potential energy is ignored because the surface deformation of the shear part is negligible. With $\theta_{w1} - \theta_s = \pi/2$ and $\theta_s - \theta_{w2} = \pi/2$, the energy $(E_K)_w^{in} +$

$(E_K)^{in}_{inter} + (E_\eta)^{in}_w$ contributed by the surface-wave eigenmodes is

$$(E_K)^{in}_w + (E_K)^{in}_{inter} + (E_\eta)^{in}_w = \frac{(a_1+a_2)^2}{2}\left(\int_0^h f^2_{uw}(y)\,\mathrm{d}y + f^2_\eta\right) - 2(a_1+a_2)\int_0^h f_{uw}(y) f_{us}(y)\,\mathrm{d}y + \frac{(a_1-a_2)^2}{2}\int_0^h f^2_{vw}(y) + f^2_{ww}(y)\,\mathrm{d}y. \tag{4.25}$$

Because a_1, a_2 and $f_{uw}(y)f_{us}(y)$ are positive and $f_{uw} < f_{ww}$, $a_1 = a_2$ minimises $(E_K)^{in}_w + (E_K)^{in}_{inter} + (E_\eta)^{in}_w$ as

$$(E_K)^{in}_w + (E_K)^{in}_{inter} + (E_\eta)^{in}_w = 2a_1^2\left(\int_0^h f^2_{uw}(y)\,\mathrm{d}y + f^2_\eta\right) - 4a_1\int_0^h f_{uw}(y) f_{us}(y)\,\mathrm{d}y, \tag{4.26}$$

which is finally determined by a_1.

Therefore, under the conditions of $a_1 = a_2$, $\theta_{w1} - \theta_s = \pi/2$ and $\theta_s - \theta_{w2} = \pi/2$, the final analytical result of P_{inter1}/E^{in} is

$$\frac{P_{inter1}}{E^{in}} = \frac{-\dfrac{a_1 F}{|\lambda_r|}\left(\sum_{n=0}^{N}\dfrac{\Phi^{(n)}(0)}{n!}t^n \sin(|\lambda_r|t + \pi/2) - 1\right)}{2a_1^2\left(\int_0^h f^2_{uw}(y)\,\mathrm{d}y + f^2_\eta\right) - 4a_1\int_0^h f_{uw}(y) f_{us}(y)\,\mathrm{d}y + (E_K)^{in}_s}, \tag{4.27}$$

which is a function of a_1 and t for specified Reynolds number, Froude number and wavenumber. For the maximum P_{inter1}/E^{in}, the value of a_1 can be obtained from $\partial(P_{inter1}/E^{in})/\partial a_1 = 0$.

Note that when $a_1 = a_2$, $\theta_{w1} - \theta_s = \pi/2$ and $\theta_s - \theta_{w2} = \pi/2$, the velocities and surface elevation perturbations of the surface-wave part satisfy

$$u_w = -2a_1 f_{uw}(y)\cos(\beta z + \theta_s)\cos(|\lambda_r|t)\mathrm{e}^{\lambda_i t}, \tag{4.28}$$

$$v_w = -2a_1 f_{vw}(y)\cos(\beta z + \theta_s)\sin(|\lambda_r|t)\mathrm{e}^{\lambda_i t}, \tag{4.29}$$

$$w_w = 2a_1 f_{ww}(y)\sin(\beta z + \theta_s)\sin(|\lambda_r|t)\mathrm{e}^{\lambda_i t}, \tag{4.30}$$

$$\eta = 2a_1 f_\eta \cos(\beta z + \theta_s)\cos(|\lambda_r|t)\mathrm{e}^{\lambda_i t}, \tag{4.31}$$

which represent a standing wave, as shown in figures 15(*c* i)–15(*c* vii).

4.1.4. *Effects of the spanwise wavenumber and Froude number at different Reynolds numbers*

The above analyses indicate that the free surface enhances the transient growth rate through the interaction production term P_{inter} (4.11). Next, we confirm this mechanism at different spanwise wavenumbers, Froude numbers and Reynolds numbers, and explain the variation in the free-surface effect on the transient growth rate of streamwise-uniform motions with different spanwise wavenumbers and Froude numbers.

Figure 16 shows a comparison of the time histories of the interaction production term P_{inter} at different Froude numbers and spanwise wavenumbers for $Re_\tau = 180$, 360 and 1000. The term P_{inter} increases with increasing Fr_τ but decreases sharply with increasing

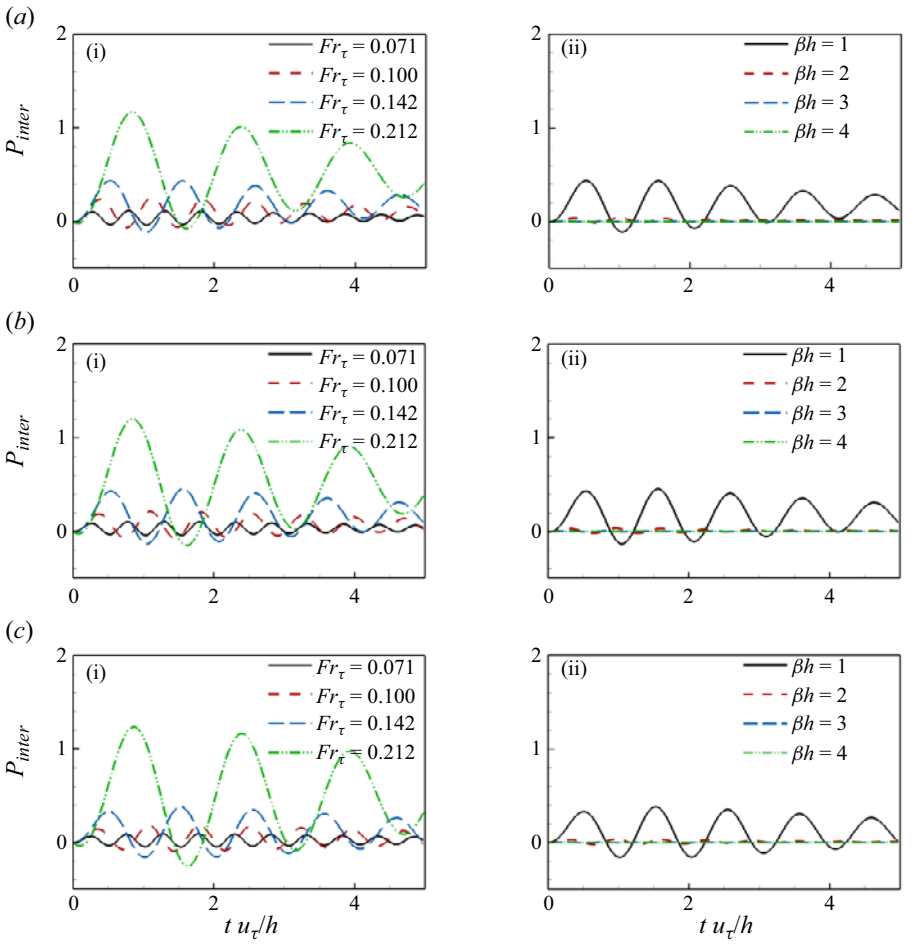

Figure 16. Time evolution of the interaction production term P_{inter} (*a* i–*c* i) at different Froude numbers Fr_τ for $\alpha h = 0$ and $\beta h = 1$ and (*a* ii–*c* ii) at different spanwise wavenumbers βh for $Fr_\tau = 0.142$ and $\alpha h = 0$. The results are obtained at (*a* i,*a* ii) $Re_\tau = 180$, (*b* i,*b* ii) $Re_\tau = 360$ and (*c* i,*c* ii) $Re_\tau = 1000$.

spanwise wavenumber βh. For the same Froude number and spanwise wavenumber, the change in P_{inter} with the Reynolds number is negligible. Recall that at three different Reynolds numbers $Re_\tau = 180$, 360 and 1000, the free-surface effects on the transient growth rate are similar (figures 5 and 7), increasing with increasing Froude number but attenuating obviously with increasing spanwise wavenumber. Thus, the variation in P_{inter} with the Froude number and spanwise wavenumber is consistent with the variation in the transient growth rate with these parameters, confirming that the interaction production term is an important mechanism underlying that the free surface influences the transient growth of motions.

The variations in P_{inter} and the transient growth rate with the Froude number and spanwise wavenumber can be explained using the analytical expression of the production term (4.27). The interaction production term P_{inter} decreases as the frequency of the surface-wave eigenmodes $|\lambda_r|$ increases. Additionally, P_{inter} in (4.27) is proportional to the integral term F (4.22) associated with the vertical velocity modulus of the surface-wave eigenmodes. The variations in the frequency and vertical velocity modulus

of the surface-wave eigenmodes with the Froude number and spanwise wavenumber are shown in figure 17. The frequency of the surface-wave eigenmodes decreases with increasing Froude number, whereas the vertical velocity modulus does not change with the Froude number. Therefore, an increase in the Froude number leads to an increase in P_{inter} (figure 16*a* i–*c* i), and this escalation can be attributed solely to the decrease in the frequency of the surface-wave eigenmodes $|\lambda_r|$. Moreover, an increase in the spanwise wavenumber has dual effects on the surface-wave eigenmodes, increasing their frequency while also reducing the integral term F. The integral term F is determined by the product of the streamwise velocity, which is composed of shear eigenmodes, and the vertical velocity, which is composed of surface-wave eigenmodes. As the spanwise wavenumber increases, the moduli of the vertical velocity of the surface-wave eigenmode becomes more concentrated near the free surface and rapidly diminishes away from it. Simultaneously, in the present result (figure 15*b* i–*b* vii) and other canonical wall-bounded turbulence (Cossu *et al.* 2009), the streamwise velocity of the perturbation composed of shear eigenmodes is more concentrated near the bottom wall. Consequently, the vertical locations where both components are significant start to separate, leading to a reduction in their product and thus a decrease in F. Combining with the increase of $|\lambda_r|$, P_{inter} decreases with increasing spanwise wavenumber (figures 16*a* ii–*c* ii). Thus, the effect of the free surface on the transient growth rate is significant only for small spanwise wavenumbers at relatively high Froude numbers.

In summary, the free surface affects the transient growth process of streamwise-uniform motions through the interaction between spanwise standing waves consisting of surface-wave eigenmodes and streamwise vortices consisting of shear eigenmodes. In particular, the growth rates of the total energy and kinetic energy are enhanced by the energy extracted from the mean velocity gradient through the correlation between the streamwise velocity induced by the lifting-up effect of the streamwise vortices and the vertical velocity induced by the spanwise standing wave. This occurs if the initial surface elevation of the standing wave is at its maximum and the phase is the same as that of the streamwise velocity induced by the lifting-up effect of the streamwise vortices. The maximal transient growth rate is inversely proportional to the frequency of the standing wave, which decreases with increasing Froude number, but increases with increasing spanwise wavenumber. In the transient growth process, only the energy of the streamwise velocity is amplified, which is at the expense of the attenuation of the streamwise vortices and standing waves. Because the initial flow field tends to trigger the transient growth, the amplified flow field represents commonly observed flow states in turbulence. The amplified flow field is featured by energetic very-large-scale u and relatively weak v and w, which is consistent with the results of direct numerical simulations and laboratory experiments of free-surface open channel turbulent flows (Borue *et al.* 1995; Kumar, Gupta & Banerjee 1998; Duan *et al.* 2020; Yoshimura & Fujita 2020).

4.2. *Effects of the free surface on streamwise-varying motions*

The analyses in § 4.1 reveal the mechanism by which the free surface influences the streamwise-uniform motions. As shown in § 3, the maximum growth rate G_{max} in the streamwise-varying case ($\alpha h \neq 0$) is also enhanced by the free surface, although its value is smaller than that of the streamwise-uniform case ($\alpha h = 0$). In this section, the case with $\alpha h = 0.2$ and $\beta h = 1$ is used as an example to elucidate the reason underlying this result. First, the effects of the surface-wave eigenmodes on the energy growth are analysed. Then, the conditions of the surface wave part and the shear part for enhancing G_{max} are derived based on the features of the surface-wave and shear eigenmodes. The following analyses

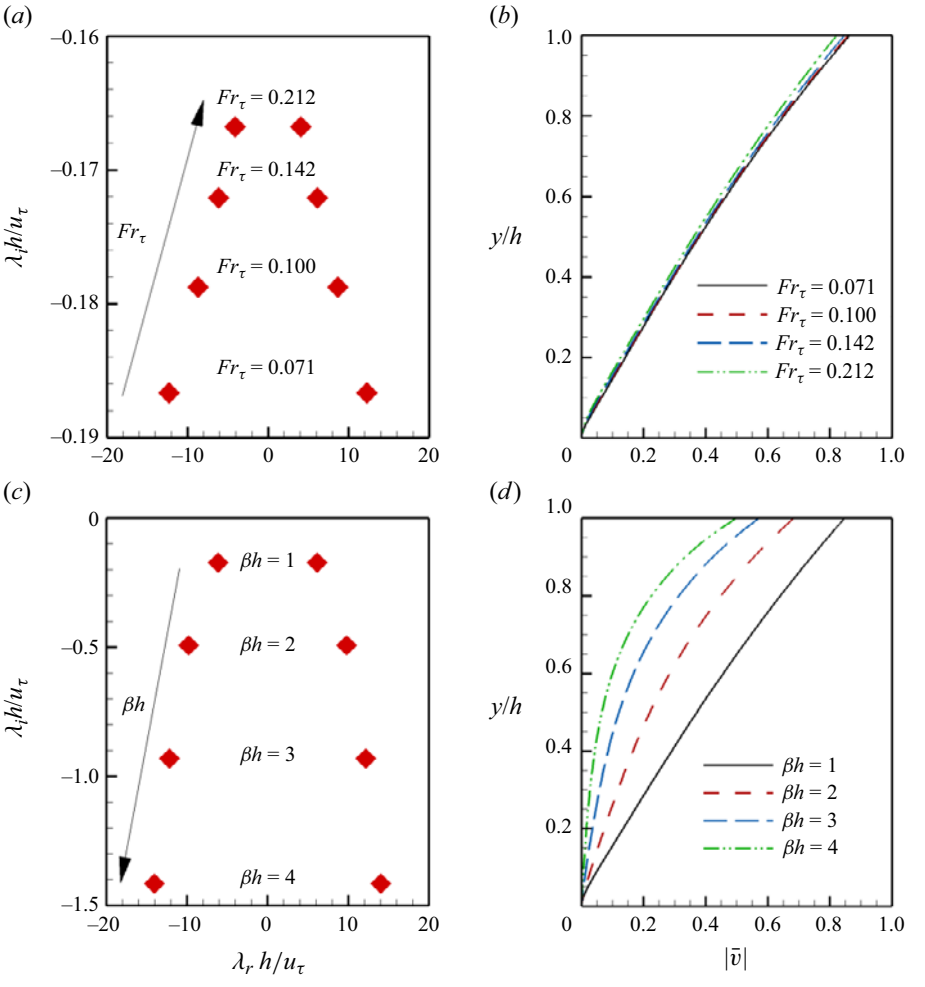

Figure 17. Variations in (*a*,*c*) the eigenvalues and (*b*,*d*) the vertical velocity modulus of the surface-wave eigenmodes (*a*,*b*) with the Froude number Fr_τ ($Fr_\tau = 0.071, 0.1, 0.142$ and 0.212) for $\alpha h = 0$ and $\beta h = 1$ and (*c*,*d*) with the spanwise wavenumber βh ($\beta h = 1$, 2, 3 and 4) for $Fr_\tau = 0.142$ and $\alpha h = 0$. The results are obtained at $Re_\tau = 180$.

elucidate the mechanism by which the free surface influences the streamwise-varying motions. In addition, we have confirmed the mechanism for the streamwise-varying motions cases across different wavenumbers, Froude numbers and Reynolds numbers in a manner similar to that for the streamwise-uniform case in § 4.1.4 (see the confirmation by the results at $\alpha h = 0.5$, $\beta h = 1$ and $Re_\tau = 6000$ in Appendix C).

4.2.1. *Effect of the free surface on the energy budgets for the streamwise-varying case*
Similar to the streamwise-uniform case analysed in § 4.1, the energy growth rate $E(t)/E^{in}$ in the streamwise-varying case is dominated by the difference between the production term and the dissipation term. According to (4.7) and (4.9), the budget terms can be decomposed into a shear part, a wave part and an interaction part, with the latter two associated with the free surface. To examine the net contribution of these three parts to $E(t)/E^{in}$, figure 18(*a*) illustrates the time evolution of the combination of the shear parts of the production term

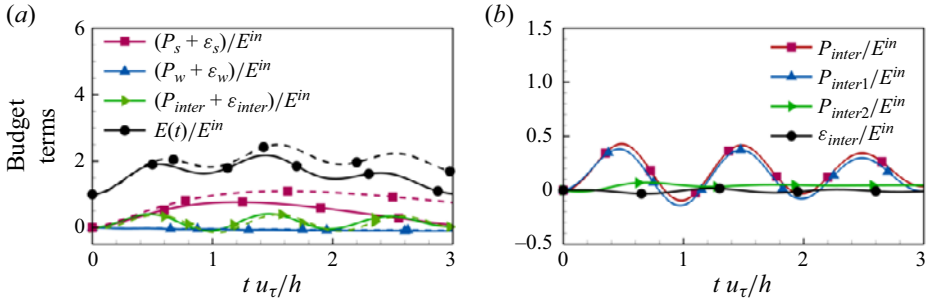

Figure 18. (*a*) Comparison of the time evolution of the budget terms $(P_s+\epsilon_s)/E^{in}$, $(P_w+\epsilon_w)/E^{in}$, $(P_{inter}+\epsilon_{inter})/E^{in}$ and $E(t)/E^{in}$ (definitions provided in § 4.1.2) between the streamwise-uniform case ($\alpha h=0$, dashed lines with symbols) and the streamwise-varying case ($\alpha h=0.2$, solid lines with symbols). (*b*) Time evolution of the budget terms P_{inter}, P_{inter1}, P_{inter2} and ϵ_{inter} in the streamwise-varying case ($\alpha h=0.2$). The results are obtained at $Re_\tau=180$, $\beta h=1$ and $Fr_\tau=0.142$.

and dissipation term $(P_s+\epsilon_s)/E^{in}$, the combination of the wave parts of the production term and dissipation term $(P_w+\epsilon_w)/E^{in}$, and the combination of the interaction parts of the production term and dissipation term $(P_{inter}+\epsilon_{inter})/E^{in}$ in the streamwise-uniform case (dashed line with symbols) and the streamwise-varying case (solid line with symbols). As shown, for both the streamwise-varying and streamwise-uniform cases, the net contribution of the wave part is negligible, while the interaction part $(P_{inter}+\epsilon_{inter})/E^{in}$ has a significant positive contribution. As shown in figure 18(*b*), the net contribution of $(P_{inter}+\epsilon_{inter})/E^{in}$ is due mainly to P_{inter}. Further decomposing P_{inter} into P_{inter1} and P_{inter2}, as shown in (4.10), we find that P_{inter} is governed by P_{inter1}. Therefore, similar to the streamwise-uniform case, the free surface enhances the energy growth rate of the streamwise-varying motions through the energy production term that arises due to the correlation between the streamwise velocity of the shear part and the vertical velocity of the surface-wave part (4.11).

Because the values of $(P_{inter}+\epsilon_{inter})/E^{in}$ in the streamwise-varying and streamwise-uniform cases in figure 18(*a*) are comparable, the energy growth rate $E(t)/E^{in}$ in the streamwise-varying case is smaller than that in the streamwise-uniform case, mainly due to the smaller net contribution from the shear part $(P_s+\epsilon_s)/E^{in}$. In closed channel flows, the energy growth rate, which is governed by the difference between the shear parts of the production and dissipation terms, also decreases with increasing αh (Cossu *et al.* 2009).

4.2.2. *Initial conditions for the transient growth of streamwise-varying motions*

Next, the features of the surface-wave part and shear part in the streamwise-varying case are analysed to study the initial state of the surface-wave part, which can lead to the maximum production term P_{inter1}/E^{in} that is responsible for the enhancement of the energy growth rate by the free surface.

Figure 19 shows the eigenvalues of the surface-wave and shear eigenmodes, and the velocity moduli of the two surface-wave eigenmodes. As shown in figure 19(*a*), there are two surface-wave eigenmodes with different λ_r, indicating different propagation speeds $c=\lambda_r/k$ along the wavenumber direction $(\alpha/k,\beta/k)$. The propagation speeds of the two surface-wave eigenmodes are $c_1=c_s+c_w$ and $c_2=c_s-c_w$, with $c_s=(\lambda_{r1}+\lambda_{r2})/(2k)=\lambda_r^s/k$ and $c_w=|\lambda_{r1}-\lambda_{r2}|/(2k)=\lambda_r^w/k$. The velocity c_s is approximately equal to the projection of the surface base flow speed in the wavenumber direction $U(h)\alpha/k$. In addition, the λ_r values of the shear eigenmodes are all close to λ_r^s, implying

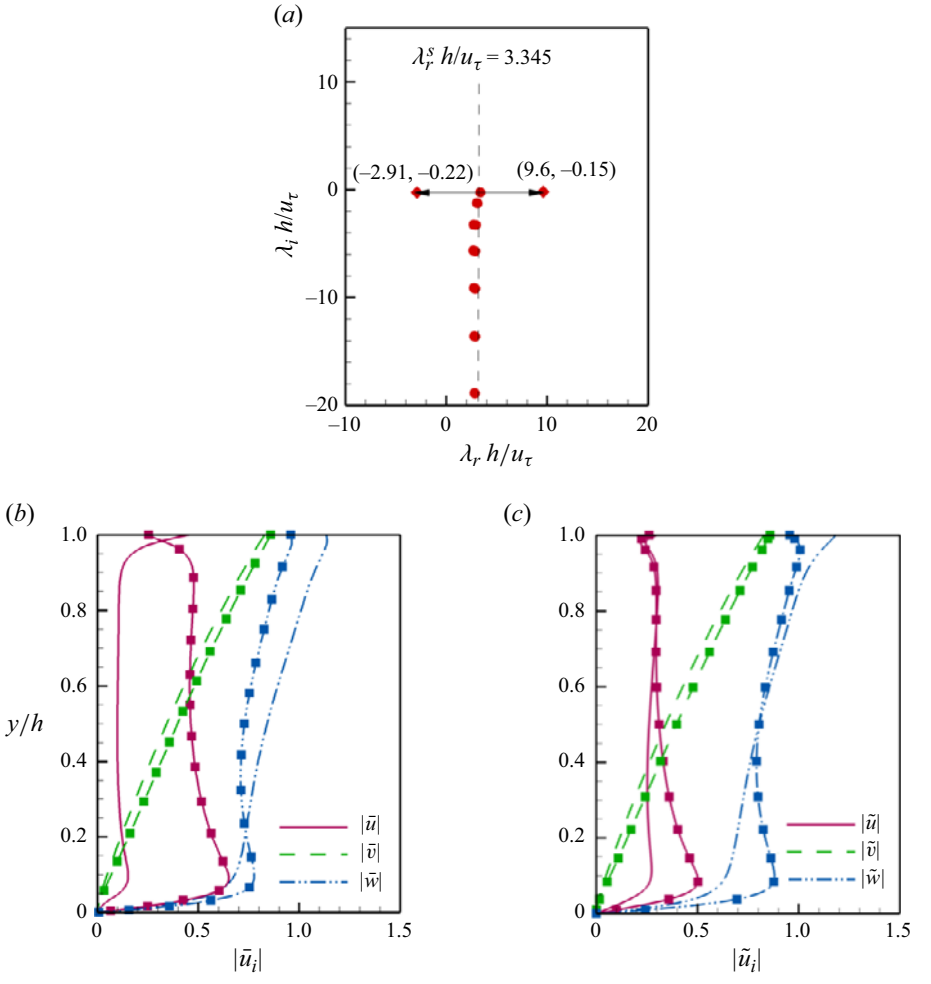

Figure 19. (*a*) Eigenvalues of the surface-wave eigenmodes (diamonds) and the shear eigenmodes (circles). (*b*,*c*) Velocity moduli of the two surface-wave eigenmodes. The surface-wave eigenmode with the larger λ_r is shown by lines without symbols, and the other eigenmode is shown by lines with symbols. The velocity moduli are shown in the coordinate system (*b*) (x, y, z) and (*c*) $(\tilde{x}, \tilde{y}, \tilde{z})$. The results are obtained at $Re_\tau = 180$, $\alpha h = 0.2$, $\beta h = 1$ and $Fr_\tau = 0.142$.

that the shear part consisting of the shear eigenmodes propagates in the direction of $(\alpha/k, \beta/k)$ at a speed of $c_s = \lambda_r^s/k$. The velocity c_w represents the propagation speed of the surface-wave eigenmodes relative to the shear eigenmodes.

Based on the propogation directions of the surface-wave eigenmodes and shear eigenmodes, a new coordinate system is defined using the transformation

$$\tilde{x} = x\frac{\beta}{k} - z\frac{\alpha}{k}, \quad \tilde{y} = y, \quad \tilde{z} = z\frac{\beta}{k} + x\frac{\alpha}{k}. \tag{4.32}$$

Here, the $\tilde{z}$-axis is parallel to the wavenumber vector. Correspondingly, the velocity components $\tilde{u}_i$ in the new coordinate system $(\tilde{x}, \tilde{y}, \tilde{z})$ are

$$\tilde{u} = u\frac{\beta}{k} - w\frac{\alpha}{k}, \quad \tilde{v} = v, \quad \tilde{w} = w\frac{\beta}{k} + u\frac{\alpha}{k}. \tag{4.33}$$

As shown in figure 19(*b*), in the coordinate system (x, y, z), the vertical velocity moduli of the two surface-wave eigenmodes are similar, while the streamwise velocity moduli of the two surface-wave eigenmodes are noticeably different. However, in the new coordinate system $(\tilde{x}, \tilde{y}, \tilde{z})$, the streamwise velocity moduli $|\tilde{u}|$ of the two eigenmodes in the $\tilde{x}$-direction are much closer (figure 19*c*).

The difference between the exponential damping rates of the two surface-wave eigenmodes, i.e. $\mathrm{e}^{\lambda_{i1}t}$ and $\mathrm{e}^{\lambda_{i2}t}$ (figure 19*a*), is small within the time needed to reach the maximum transient growth rate ($t_{max} \approx 1.5h/u_\tau$). Therefore, the velocity of the surface-wave part can be approximated as

$$\tilde{u}_w = a_1 f_{\tilde{u}w} \sin(k\tilde{\tilde{z}} + \lambda_r^w t + \theta_{w1})\mathrm{e}^{\lambda_i t} - a_2 f_{\tilde{u}w} \sin(k\tilde{\tilde{z}} - \lambda_r^w t + \theta_{w2})\mathrm{e}^{\lambda_i t}, \tag{4.34}$$

$$\tilde{v}_w = a_1 f_{\tilde{v}w} \cos(k\tilde{\tilde{z}} + \lambda_r^w t + \theta_{w1})\mathrm{e}^{\lambda_i t} + a_2 f_{\tilde{v}w} \cos(k\tilde{\tilde{z}} - \lambda_r^w t + \theta_{w2})\mathrm{e}^{\lambda_i t}, \tag{4.35}$$

$$\tilde{w}_w = -a_1 f_{\tilde{w}w} \sin(k\tilde{\tilde{z}} + \lambda_r^w t + \theta_{w1})\mathrm{e}^{\lambda_i t} - a_2 f_{\tilde{w}w} \sin(k\tilde{\tilde{z}} - \lambda_r^w t + \theta_{w2})\mathrm{e}^{\lambda_i t}, \tag{4.36}$$

$$\tilde{\eta}_w = a_1 f_\eta \sin(k\tilde{\tilde{z}} + \lambda_r^w t + \theta_{w1})\mathrm{e}^{\lambda_i t} - a_2 f_\eta \sin(k\tilde{\tilde{z}} - \lambda_r^w t + \theta_{w2})\mathrm{e}^{\lambda_i t}. \tag{4.37}$$

Here, $f_{\tilde{u}w}, f_{\tilde{v}w}, f_{\tilde{w}w}, f_\eta$ and λ_i are approximations of the moduli of $\tilde{u}$, $\tilde{v}$, $\tilde{w}$, η and the damping rate of the two surface-wave eigenmodes, respectively, and

$$\tilde{\tilde{z}} = \tilde{z} - c_s t. \tag{4.38}$$

The two surface-wave eigenmodes in the streamwise-varying case propagate in opposite $\tilde{\tilde{z}}$-directions at the same phase speed; hence, the surface-wave part has a similar expression to that in the streamwise-uniform case (4.17)–(4.20).

Figure 20 displays the flow field and surface deformation in the transient growth process in the plane $(\tilde{y} = y, \tilde{\tilde{z}} = \tilde{z} - c_s t)$, as well as the corresponding shear and surface-wave parts, at $t = iT/4$, with $i = 0, 1, \ldots, 6$. Here, the period T is equal to $2\pi/(kc_w)$, and the velocity c_w is the propagation speed of the surface-wave eigenmode relative to the speed of the shear eigenmodes (figure 19*a*). As shown in figure 20(*b* i–*b* vii), the shear part consists of initially strong vortices in the $\tilde{x}$-direction, as evidenced by $(\tilde{v}, \tilde{w})$ and the streaks of $\tilde{u}$. As time increases, the vortices decay and the streaks are enhanced. Because the phase speed of the shear eigenmodes in the wavenumber vector direction is approximately c_s (figure 19*a*), the spanwise locations of the vortices are essentially unchanged in the plane $(\tilde{y} = y, \tilde{\tilde{z}} = \tilde{z} - c_s t)$. As a result, the velocities of the shear part can be approximated as

$$\tilde{u}_s = f_{\tilde{u}s}(\tilde{y}) \cos(k\tilde{\tilde{z}} + \theta_s)\tilde{g}(t), \tag{4.39}$$

$$\tilde{v}_s = -f_{\tilde{v}s}(\tilde{y}) \cos(k\tilde{\tilde{z}} + \theta_s)\tilde{m}(t), \tag{4.40}$$

$$\tilde{w}_s = -f_{\tilde{w}s}(\tilde{y}) \sin(k\tilde{\tilde{z}} + \theta_s)\tilde{n}(t), \tag{4.41}$$

with $\tilde{g}(t) \geq 1$, $\tilde{m}(t) \leq 1$ and $\tilde{n}(t) \leq 1$. The moduli $f_{\tilde{u}s}$ and $f_{\tilde{v}s}$ are positive, while the sign of $f_{\tilde{w}s}(y)$ changes near the channel centre. The shear part in the streamwise-varying case, expressed using $\tilde{y}$ and $\tilde{\tilde{z}}$, is similar to that in the streamwise-uniform case (4.14)–(4.16).

Here, P_{inter1} can be expressed as

$$P_{inter1} = \int_0^h \int_0^t \overline{\tilde{u}_s \tilde{v}_w} U' \,\mathrm{d}t \,\mathrm{d}y = \int_0^h \int_0^t \left(\frac{\beta}{k} \overline{\tilde{u}_s \tilde{v}_w} + \frac{\alpha}{k} \overline{\tilde{w}_s \tilde{v}_w} \right) U' \,\mathrm{d}t \,\mathrm{d}y$$

$$\approx \int_0^h \int_0^t \frac{\beta}{k} \overline{\tilde{u}_s \tilde{v}_w} U' \,\mathrm{d}t \,\mathrm{d}y. \tag{4.42}$$

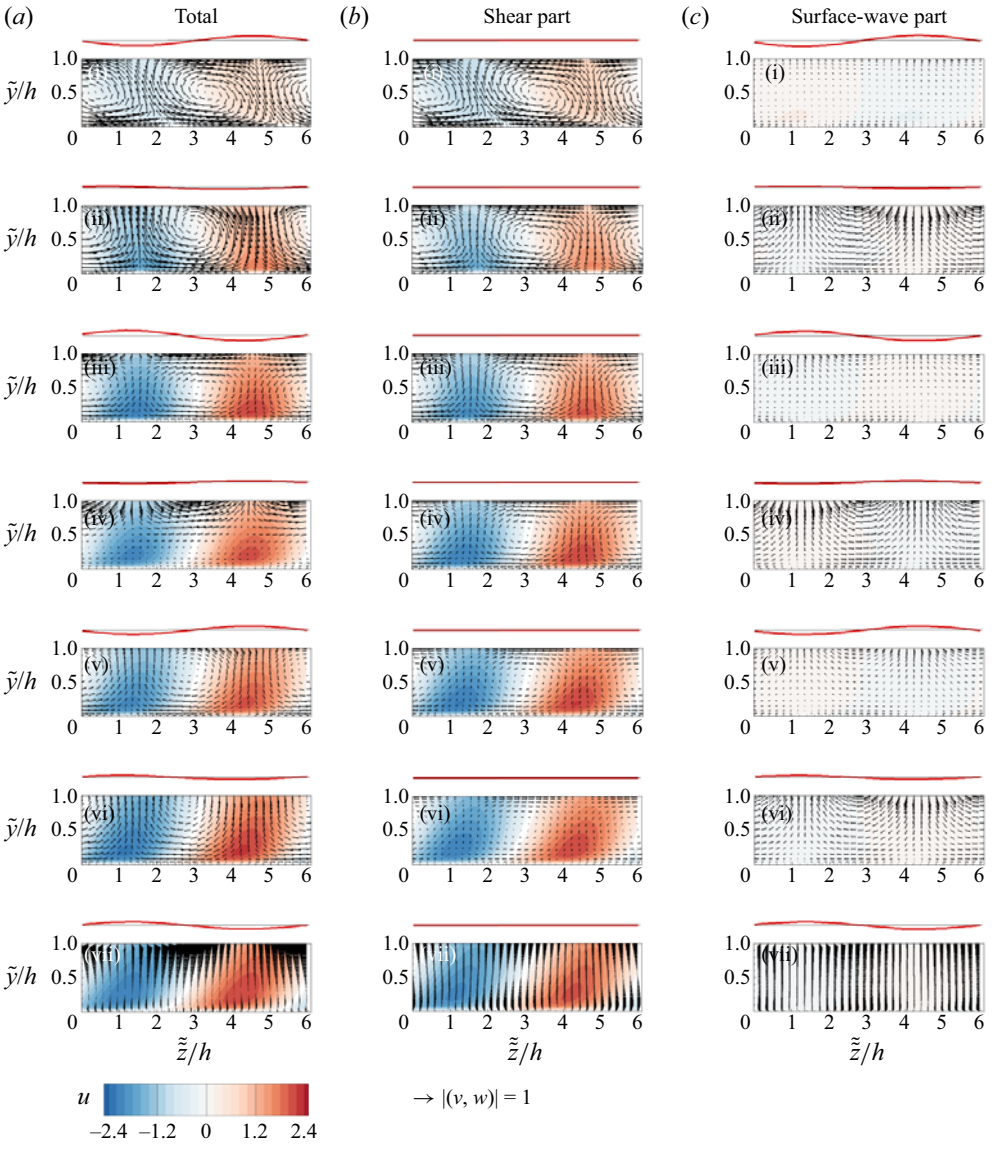

Figure 20. Velocity field $(\tilde{u}, \tilde{v}, \tilde{w})$ and the surface elevation η, as well as their shear and surface-wave parts, in the plane $(\tilde{y} = y, \tilde{\tilde{z}} = \tilde{z} - c_s t)$ at (*a* i–*c* i) $t = 0$, (*a* ii–*c* ii) $t = T/4$, (*a* iii–*c* iii) $t = T/2$, (*a* iv–*c* iv) $t = 3T/4$, (*a* v–*c* v) $t = T$, (*a* vi–*c* vi) $t = 5T/4$ and (*a* vii–*c* vii) $t = 3T/2$. Panels (*a* i–*a* vii) show the total, panels (*b* i–*b* vii) depict the shear part and panels (*c* i–*c* vii) display the surface-wave part. Here, T is equal to $2\pi/(kc_w)$, where c_w is the propagation speed of the surface-wave eigenmodes relative to that of the shear eigenmodes, and the maximum transient growth rate is reached at $t = 3T/2$. The vector is composed of the vertical and spanwise velocities $(\tilde{v}, \tilde{w})$, and the contours are the streamwise velocity $\tilde{u}$. The results are obtained at $Re_\tau = 180$, $\alpha h = 0.2$, $\beta h = 1$ and $Fr_\tau = 0.142$.

Because the sign of $\tilde{w}_s$ changes in the y (or $\tilde{y}$) direction and the sign of $\tilde{v}_w$ remains the same in the y direction, the integral $\alpha\overline{\tilde{w}_s\tilde{v}_w}/k$ in the y direction is negligible. Additionally, α is much smaller than β for streamwise-elongated motions, which we focus on in the present study. Therefore, the $\alpha\overline{\tilde{w}_s\tilde{v}_w}/k$ part is ignored. Because $\tilde{u}_s$ and $\tilde{v}_w$ in (4.39) and (4.34) have

the same forms as those in the streamwise-uniform case, we obtain following (4.21) that

$$P_{inter1} \approx \frac{\beta}{k}\left(-\frac{1}{2}\tilde{F}\sum_{n=0}^{N}\frac{\tilde{\Phi}^n(0)}{|\lambda_r^w|n!}t^n(a_1\sin(\lambda_r^w t+\theta_{w1}-\theta_s)+a_2\sin(\lambda_r^w t+\theta_s-\theta_{w2}))\right)$$
$$+\frac{\beta}{k}\frac{a_1\tilde{F}\sin(\theta_{w1}-\theta_s)+a_2\tilde{F}\sin(\theta_s-\theta_{w2})}{2|\lambda_r^w|}, \tag{4.43}$$

with

$$\tilde{F}=\int_0^h f_{\tilde{u}s}(y)f_{\tilde{v}w}(y)U'\,\mathrm{d}y \tag{4.44}$$

and

$$\tilde{\Phi}(t)=\tilde{g}(t)\mathrm{e}^{\lambda_i t}. \tag{4.45}$$

Similar to the streamwise-uniform case, the maximum value of P_{inter1} is obtained when $\theta_{w1}-\theta_s=\pi/2$ and $\theta_s-\theta_{w2}=\pi/2$ are satisfied. Under this condition, the portion of the initial input energy associated with the surface-wave part is

$$(E_K)_w^{in}+(E_K)_{inter}^{in}+(E_\eta)_w^{in}=\frac{(a_1+a_2)^2}{2}\left(\int_0^h f_{\tilde{u}w}^2(y)\,\mathrm{d}y+f_\eta^2\right)$$
$$-2(a_1+a_2)\int_0^h f_{\tilde{u}w}(y)f_{\tilde{u}s}(y)\,\mathrm{d}y+\frac{(a_1-a_2)^2}{2}\int_0^h\left(f_{\tilde{v}w}^2(y)+f_{\tilde{w}w}^2(y)\right)\mathrm{d}y. \tag{4.46}$$

The minimum value is obtained when $a_1\approx a_2$. Because the moduli of the two surface-wave eigenmodes are only approximately the same, i.e. not identical, a_1 is not exactly equal to a_2.

The above analyses show that in the streamwise-varying case, the maximum P_{inter1}/E^{in} is obtained when $a_1\approx a_2$, $\theta_{w1}-\theta_s=\pi/2$ and $\theta_s-\theta_{w2}=\pi/2$. Under these conditions, the velocities and surface elevation of the surface-wave part are

$$\tilde{u}_w\approx -2a_1 f_{\tilde{u}w}(y)\cos(k\tilde{\tilde{z}}+\theta_s)\cos(|\lambda_r^w|t)\mathrm{e}^{\lambda_i t}, \tag{4.47}$$

$$\tilde{v}_w\approx -2a_1 f_{\tilde{v}w}(y)\cos(k\tilde{\tilde{z}}+\theta_s)\sin(|\lambda_r^w|t)\mathrm{e}^{\lambda_i t}, \tag{4.48}$$

$$\tilde{w}_w\approx 2a_1 f_{\tilde{w}w}(y)\sin(k\tilde{\tilde{z}}+\theta_s)\sin(|\lambda_r^w|t)\mathrm{e}^{\lambda_i t} \tag{4.49}$$

and

$$\eta\approx 2a_1 f_\eta\cos(k\tilde{\tilde{z}}+\theta_s)\cos(|\lambda_r^w|t)\mathrm{e}^{\lambda_i t}. \tag{4.50}$$

This solution represents a standing wave in the plane $(\tilde{y},\tilde{\tilde{z}})$ parallel to the wavenumber vector that moves with speed c_s in the wavenumber-vector direction. Initially, the surface elevation of the standing wave is at its maximum value, and its phase is the same as that of $\tilde{u}_s$. The standing wave can be confirmed by the variation in the surface elevation at different times, as shown in figure 20(*c* i–*c* vii).

In summary, the above analyses show that for the streamwise-varying case, in a plane parallel to the wavenumber vector moving at a speed equal to the surface mean velocity projected in the wavenumber-vector direction, the two surface-wave eigenmodes propagate in opposite directions at the same speed, and the vortices consisting of the shear eigenmodes are approximately fixed in space. If a standing wave reaches its maximum surface elevation and its phase is identical to that of the streamwise velocity induced by

the lifting-up effect of the vortices at the initial time, the transient growth rate can be enhanced by the free surface to a maximal level. In other words, the transient growth rate is enhanced by a standing wave riding on the vortices moving at a speed equal to the projection of the surface mean velocity in the wavenumber direction. While the interaction between the surface-wave part and the shear part can enhance the transient growth rate of the streamwise-varying motions in a way similar to that of streamwise-uniform motions, the growth of the total perturbation energy of the streamwise-varying motions is slower because of the decrease in the transient growth rate of the shear part with increasing streamwise wavenumber.

5. Conclusions

In this study, a linear non-modal analysis is performed to investigate the linear mechanism by which free surfaces influence turbulent motions in open channels with a deformable free surface. We use the generalised Orr–Sommerfeld and Squire equations derived from the Reynolds-averaging equation, with the turbulent mean velocity and eddy viscosity included, in our analyses; therefore, the effects of background turbulence are considered in the present study. Because of the transformation of surface potential energy into kinetic energy in the flow, the growth rate of the total energy is considered. The growth rate is calculated by discretising the generalised Orr–Sommerfeld and Squire equations using a Chebyshev spectral collocation method. The results at $Re_\tau = 180$, 360, 1000 and 6000 are analysed to elucidate the mechanism by which the free surface influences the transient growth rate.

As observed from the contours of the maximum energy growth rate G_{max} in the spectral space, the G_{max} value of the streamwise-elongated motions (for which the streamwise wavenumber αh is smaller than the spanwise wavenumber βh) at small spanwise wavenumbers $\beta h < 2.7$ is amplified by the free surface at relatively high Froude numbers. This effect is more obvious when the wavenumber decreases and the Froude number increases. The growth rate of the kinetic energy E_K corresponding to G_{max} is also amplified by the free surface. There are two additional surface-wave eigenmodes in the free-surface open channel case compared with the rigid-lid open channel case. If the surface-wave eigenmodes are ignored, G_{max} in the free-surface open channel is the same as that in the rigid-lid open channel, indicating that the surface-wave eigenmodes are important in the enhancement of G_{max}.

The budget equation for the energy growth rate is derived to elucidate the mechanism by which the surface-wave eigenmodes influence the growth rate. The budget analysis indicates that the energy growth rate is determined by the difference between the energy production term and the dissipation term, and the surface energy transfer term is negligible. By decomposing the perturbation term into a shear part consisting of the shear eigenmodes and a surface-wave part consisting of the surface-wave eigenmodes, we discover that the increase in G_{max} is due to the interaction term P_{inter}, which involves the correlation between the shear part of the streamwise velocity and the surface-wave part of the vertical velocity. The interaction production term exists owing to the non-orthogonality of the eigenmodes.

In the streamwise-uniform case ($\alpha h = 0$), the initial shear part of the flow field consists of a pair of streamwise vortices and relatively weak streaks of streamwise velocity that do not move in the spanwise direction over time, similar to other canonical wall-bounded turbulent flows without free surfaces. The two surface-wave eigenmodes propagate in opposite directions along the spanwise axis. Based on the characteristics of the shear eigenmodes and the surface-wave eigenmodes, an analytical expression of the interaction

energy production term is derived (4.27). The maximum value of the interaction energy production term is obtained when the surface wave is a standing wave, for which the surface elevation is initially at its maximum value and the spanwise phase is the same as that of the shear part of the streamwise velocity. According to the derived analytical expression of the interaction energy production term, the increase in G_{max} due to the free surface becomes more pronounced when the frequency of the surface-wave eigenmodes decreases. When the Froude number increases or the spanwise wavenumber decreases, the frequency of the surface-wave eigenmodes decreases. Therefore, the free surface has more pronounced effects at large Froude numbers and small spanwise wavenumbers.

For the streamwise-varying case ($\alpha h \neq 0$), the shear part of the flow field also consists of a pair of streamwise vortices and relatively weak streaks of streamwise velocity moving at a speed c_s, which is approximately the same as the projection of the surface base flow speed in the wavenumber direction. We define a new coordinate system $(\tilde{x}, \tilde{y}, \tilde{z})$ with its spanwise-axis $\tilde{z}$ along the wavenumber direction. In the plane $(\tilde{y}, \tilde{z} - c_s t)$, i.e. the plane moving with the streamwise vortices and streaks at a speed of c_s, the two surface-wave eigenmodes propagate in opposite directions along the $\tilde{z}$-axis at the same speed, and the spanwise location of the shear part remains fixed over time. Similar to the streamwise-uniform case, it is also proven that in the moving plane, a standing wave riding on the streamwise vortices can lead to the maximum energy growth rate, provided that the surface elevation of the standing wave is maximised at the initial time and the spanwise phase is the same as that of the shear part of the streamwise velocity.

Finally, we remark that although the present study reveals only a linear mechanism, our results are consistent with the observations from direct numerical simulations and laboratory experiments. In other canonical wall-bounded turbulence problems, it has been found that linear processes are highly important for sustaining turbulence. There exists a consensus in the research community that the linear lifting-up effect, leading to the non-modal transient growth of perturbation energy, plays an important role in the generation of very-large-scale streaks, and the secondary instability of the very-large-scale streaks induced by the lift-up mechanism is linked to the generation of LSMs. The present work and the work of Camporeale *et al.* (2021) also show these two processes in open channel flows. In the free-surface open channel flows, other possible nonlinear mechanisms may also be important for wave–turbulence interactions, which should be studied in a nonlinear framework in future works.

Acknowledgements. We would like to thank the three referees for their valuable comments, which gave us significant help in improving the previous version of this paper.

Funding. The work of B.-Q.D. was supported by the NSFC project 'Investigation on dynamical mechanisms of wall turbulence based on coherent structures of different streamwise length scales' (grant no. 12302291), and the work of L.S. was supported by the University of Minnesota.

Declaration of interests. The authors report no conflict of interest.

Author ORCIDs.
Bing-Qing Deng https://orcid.org/0000-0003-1483-9694;
Zixuan Yang https://orcid.org/0000-0002-7764-3595;
Lian Shen https://orcid.org/0000-0003-3762-3829.

Appendix A. Reynolds-number effect on the time reaching the maximum transient growth in open channel flows

Figure 21 compares the time reaching the maximum transient growth rate t_{max} at different Reynolds numbers in the rigid-lid open channel flows. As shown, t_{max} is of the order

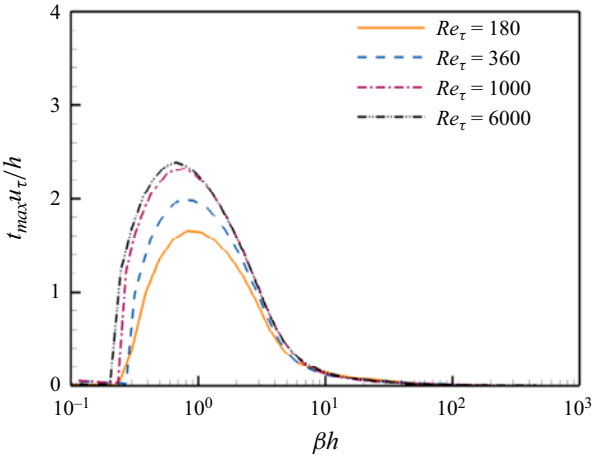

Figure 21. Comparison of the time reaching the maximum transient growth rate t_{max} at $Re_\tau = 180$, 360, 1000 and 6000 in the rigid-lid open channel flows for $\alpha h = 0$.

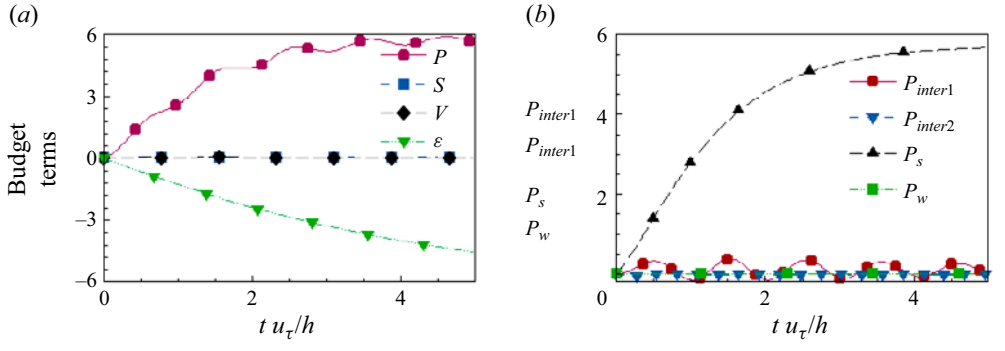

Figure 22. Time evolution of (*a*) the budget terms (4.1) and (*b*) the components of the production terms (4.7) normalised by E^{in} at $Re_\tau = 6000$ and $Fr_\tau = 0.142$ for $\alpha h = 0$ and $\beta h = 1$, with the initial input perturbations leading to G_{max}.

of h/u_τ for βh around 1, close to the growth time of very-large-scale streaks found in the direct numerical simulations of closed channel flows (Hwang & Bengana 2016). Additionally, t_{max} gradually grows with Re_τ, with its maximum value increasing from 1.8 at $Re_\tau = 180$ to 2.4 at $Re_\tau = 6000$, which is similar to that in closed channel flows (Pujals *et al.* 2009).

Appendix B. Energy budget for streamwise-uniform motions at $Re_\tau = 6000$

In this section, we confirm the mechanism of how the free surface influences streamwise-uniform motions at $Re_\tau = 6000$. Figure 22 shows the time evolution of the energy budget terms in (4.1) at $Re_\tau = 6000$ with $Fr_\tau = 0.142$, $\alpha h = 0$ and $\beta h = 1$. It can be found that the energy is mainly generated by the production term (figure 22*a*). From figure 22(*b*), we can further find that the production term is mainly contributed by the shear production P_s and the interaction production term P_{inter1}, consistent with the finding at $Re_\tau = 180$.

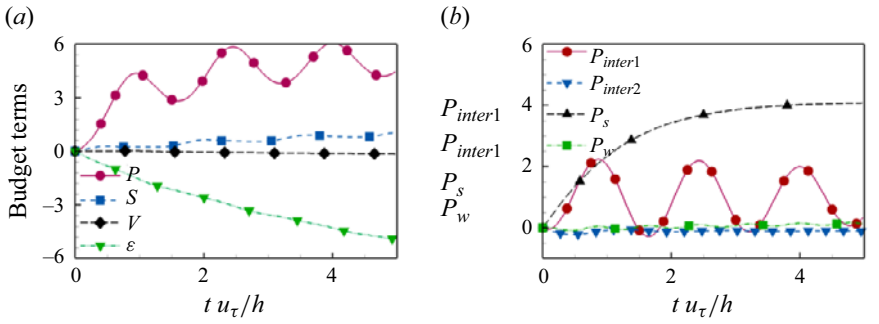

Figure 23. Time evolution of (*a*) the budget terms (4.1) and (*b*) the components of the production terms (4.7) normalised by E^{in} at $Re_\tau = 6000$ and $Fr_\tau = 0.142$ for $\alpha h = 0$ and $\beta h = 0.6$, with the initial input perturbations leading to G_{max}.

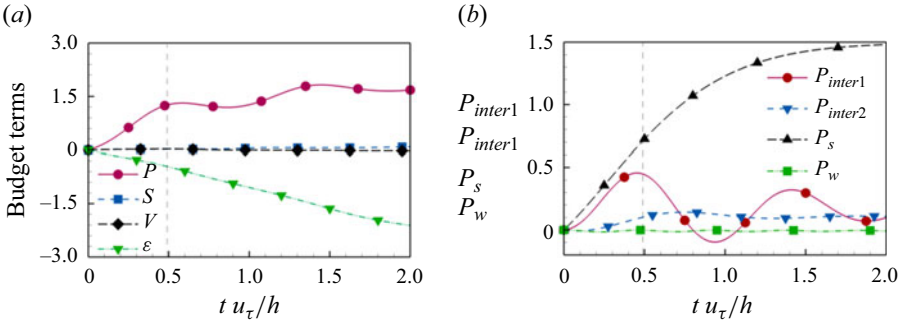

Figure 24. Time evolution of (*a*) the budget terms (4.1) and (*b*) the components of the production terms (4.7) normalised by E^{in} at $Re_\tau = 6000$ and $Fr_\tau = 0.142$ for $\alpha h = 0.5$ and $\beta h = 1$, with the initial input perturbations leading to G_{max}.

Figure 23 also shows the time evolution of the energy budget terms in (4.1) at a smaller spanwise wavenumber $\beta h = 0.6$ in the streamwise-uniform case, with the Reynolds number and the Froude number the same as those in figure 22. As shown in figure 23(*a*), although the surface term S is larger than that for $\beta h = 1$, the energy is still mainly generated by the production term (figure 23*a*). Compared with the production terms at $\beta h = 1$ (figure 22*b*), the contribution of the interaction production P_{inter1} is much larger. This is consistent with the variation tendency of P_{inter1} with βh in § 4.1.4 at lower Reynolds numbers, which is responsible for the more obvious free-surface effect at smaller βh found in § 3.

Appendix C. Confirmation of the mechanism for streamwise-varying motions at $Re_\tau = 6000$

In this section, we confirm the mechanism of how the free surface influences the streamwise-varying motions at $Re_\tau = 6000$ and $\alpha h = 0.5$, as the typical streamwise length scale of VLSMs in open channel flows is approximately $10h$ (Pinelli *et al.* 2022). As shown in figure 24, the energy is mainly provided by the production term, and the interaction production term P_{inter1} involving the vertical velocity of the surface-wave eigenmode has a significant contribution, agreeing with the finding at $\alpha h = 0.2$ and $Re_\tau = 180$.

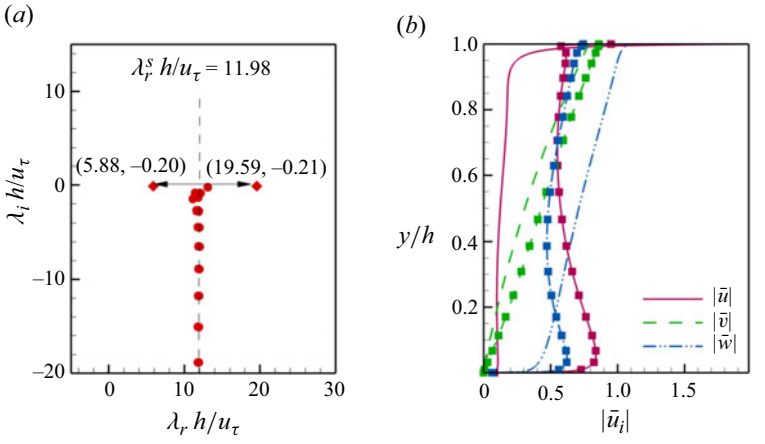

Figure 25. (*a*) Eigenvalues of the surface-wave eigenmodes (diamonds) and the shear eigenmodes (circles). (*b*) Velocity moduli of the two surface-wave eigenmodes. The surface-wave eigenmode with the larger λ_r is shown by lines without symbols, and the other eigenmode is shown by lines with symbols. The results are obtained at $Re_\tau = 3000$, $\alpha h = 0.5$, $\beta h = 1$ and $Fr_\tau = 0.142$.

Figure 25 further shows the eigenvalues and eigenmodes at $Re_\tau = 6000$ for $\alpha h = 0.5$ and $\beta h = 1$. It can be found that there are two surface-wave eigenmodes travelling downstream and upstream with respect to the shear eigenmodes that transport at the speed around $c_s = \lambda_r^s/k$. Although the streamwise and spanwise velocity components of these two surface-wave eigenmodes are different, the vertical velocity component in these two surface-wave eigenmodes are close to each other. Because P_{inter1} is related to the vertical velocity of the surface-wave eigenmodes, the derivation of P_{inter1} in § 4.2 still works.

References

Adrian, R.J. & Marusic, I. 2012 Coherent structures in flow over hydraulic engineering surfaces. *J. Hydraul. Res.* **50** (5), 451–464.

del Álamo, J.C. & Jiménez, J. 2006 Linear energy amplification in turbulent channels. *J. Fluid Mech.* **559**, 205–213.

Ambrosi, D. & Onorato, M. 2008 Non-normal stability analysis of a shear current under surface gravity waves. *J. Fluid Mech.* **609**, 49–58.

Auel, C., Albayrak, I. & Boes, R.M. 2014 Turbulence characteristics in supercritical open channel flows: effects of Froude number and aspect ratio. *ASCE J. Hydraul. Engng* **140**, 04014004.

Balakumar, B.J. & Adrian, R.J. 2007 Large- and very-large-scale motions in channel and boundary-layer flows. *Phil. Trans. R. Soc.* A **365** (1852), 665–681.

Borue, V., Orszag, S.A. & Staroselsky, I. 1995 Interaction of surface waves with turbulence: direct numerical simulations of turbulent open-channel flow. *J. Fluid Mech.* **286**, 1–23.

Brocchini, M. & Peregrine, D.H. 2001 The dynamics of strong turbulence at free surfaces. Part 1. Description. *J. Fluid Mech.* **449**, 225–254.

Burns, J.C. 1953 Long waves in running water. *Math. Proc. Camb. Phil. Soc.* **49** (4), 695–706.

Butler, K.M. & Farrell, B.F. 1992 Three-dimensional optimal perturbations in viscous shear flows. *Phys. Fluids* **4** (8), 1637–1650.

Butler, K.M. & Farrell, B.F. 1993 Optimal perturbations and streak spacing in wall-bounded turbulent shear flow. *Phys. Fluids* **5** (3), 774–777.

Calmet, I. & Magnaudet, J. 2003 Statistical structure of high-Reynolds-number turbulence close to the free surface of an open-channel flow. *J. Fluid Mech.* **474**, 355–378.

Cameron, S.M., Nikora, V.I. & Stewart, M.T. 2017 Very-large-scale motions in rough-bed open-channel flow. *J. Fluid Mech.* **814**, 416–429.

CAMPOREALE, C., CANNAMELA, F., CANUTO, C. & MANES, C. 2021 Stability analysis of open-channel flows with secondary currents. *J. Fluid Mech.* **927**, A32.

COSSU, C. & HWANG, Y. 2017 Self-sustaining processes at all scales in wall-bounded turbulent shear flows. *Phil. Trans. R. Soc.* A **375**, 20160088.

COSSU, C., PUJALS, G. & DEPARDON, S. 2009 Optimal transient growth and very large-scale structures in turbulent boundary layers. *J. Fluid Mech.* **619**, 79–94.

CRAIK, A.D.D. & LEIBOVICH, S. 1976 A rational model for Langmuir circulations. *J. Fluid Mech.* **73** (3), 401–426.

DENG, B.-Q., XU, C., HUANG, W. & CUI, G. 2013 Effect of active control on optimal structures in wall turbulence. *Sci. China Phys. Mech.* **56**, 290–297.

DENG, B.-Q., YANG, Z., XUAN, A. & SHEN, L. 2019 Influence of Langmuir circulations on turbulence in the bottom boundary layer of shallow water. *J. Fluid Mech.* **861**, 275–308.

DENG, B.-Q., YANG, Z., XUAN, A. & SHEN, L. 2020 Localizing effect of Langmuir circulations on small-scale turbulence in shallow water. *J. Fluid Mech.* **893**, A6.

DI, Y., DENG, B.Q., XUAN, A., LI, Y. & SHEN, L. 2019 Froude number effects on free surface turbulence in open channel flow. In *72nd Annual Meeting of the APS Division of Fluid Dynamics*. APS.

DIMAS, A.A. & TRIANTAFYLLOU, G.S. 1994 Nonlinear interaction of shear flow with a free surface. *J. Fluid Mech.* **260**, 211–246.

DOLCETTI, G., HOROSHENKOV, K.V., KRYNKIN, A. & TAIT, S.J. 2016 Frequency–wavenumber spectrum of the free surface of shallow turbulent flows over a rough boundary. *Phys. Fluids* **28** (10), 105105.

DUAN, Y., CHEN, Q., LI, D. & ZHONG, Q. 2020 Contributions of very large-scale motions to turbulence statistics in open channel flows. *J. Fluid Mech.* **892**, A3.

ELLINGSEN, T. & PLAM, E. 1975 Stability of linear flow. *Phys. Fluids* **18**, 487–488.

GARGETT, A., WELLS, J., TEJADA-MARTÍNEZ, A.E. & GROSCH, C.E. 2004 Langmuir supercells: a mechanism for sediment resuspension and transport in shallow seas. *Science* **306**, 1925–1928.

DE GIOVANETTI, M., SUNG, H.J. & HWANG, Y. 2017 Streak instability in turbulent channel flow: the seeding mechanism of large-scale motions. *J. Fluid Mech.* **832**, 483–513.

GUALA, M., HOMMEMA, S.E. & ADRIAN, R.J. 2006 Large-scale and very-large-scale motions in turbulent pipe flow. *J. Fluid Mech.* **554**, 521–542.

GULLIVER, J.S. & HALVERSON, M.J. 1989 Measurements of large streamwise vortices in an open-channel flow. *Water Resour. Res.* **23**, 115–123.

HANDLER, R.A., SWEAN, T.F. JR., Leighton, R.I. & Swearingen, J.D. 1993 Length scales and the energy balance for turbulence near a free surface. *AIAA J.* **31** (11), 1998–2007.

HUNT, J.C.R. 1984 Turbulence structure in thermal convection and shear-free boundary layers. *J. Fluid Mech.* **138**, 161–184.

HUNT, J.C.R. & GRAHAM, J.M.R. 1978 Free-stream turbulence near plane boundaries. *J. Fluid Mech.* **84** (2), 209–235.

HUTCHINS, N. & MARUSIC, I. 2007 Large-scale influences in near-wall turbulence. *Proc. R. Soc. Lond.* A **365** (1852), 647–664.

HWANG, Y. & BENGANA, Y. 2016 Self-sustaining process of minimal attached eddies in turbulent channel flow. *J. Fluid Mech.* **795**, 708–738.

HWANG, Y. & COSSU, C. 2010 Amplification of coherent streaks in the turbulent Couette flow: an input-output analysis at low Reynolds number. *J. Fluid Mech.* **643**, 333–348.

ILLINGWORTH, S.J., MONTY, J.P. & MARUSIC, I. 2018 Estimating large-scale structures in wall turbulence using linear models. *J. Fluid Mech.* **842**, 146–162.

JÄHNE, B. & HAUSSECKER, H. 1998 Air–water gas exchange. *Annu. Rev. Fluid Mech.* **30**, 443–468.

JIMENEZ, J. 2018 Coherent structures in wall-bounded turbulence. *J. Fluid Mech.* **842**, P1.

KERMANI, A., KHAKPOUR, H.R., SHEN, L. & IGUSA, T. 2011 Statistics of surface renewal of passive scalars in free-surface turbulence. *J. Fluid Mech.* **678**, 379–416.

KIM, K.C. & ADRIAN, R.J. 1999 Very large-scale motion in the outer layer. *Phys. Fluids* **11** (2), 417–422.

KOMORI, S., MURAKAMI, Y. & UEDA, H. 1989 The relationship between surface-renewal and bursting motions in open-channel flow. *J. Fluid Mech.* **203**, 103–123.

KOMORI, S., NAGAOSA, R. & MURIKAMI, Y. 1993 Direct numerical simulation of three-dimensional open-channel flow with zero-shear gas–liquid interface. *Phys. Fluids* **5** (1), 115–125.

KUMAR, S., GUPTA, R. & BANERJEE, S. 1998 An experimental investigation of the characteristics of free-surface turbulence in channel flow. *Phys. Fluids* **10** (2), 437–456.

LAM, K. & BANERJEE, S. 1992 On the condition of streak formation in a bounded turbulent flow. *Phys. Fluids* **4** (2), 306–320.

LEGLEITER, C.J., MOBLEY, C.D. & OVERSTREET, B.T. 2017 A framework for modeling connections between hydraulics, water surface roughness, and surface reflectance in open channel flows. *J. Geophys. Res. Earth Surf.* **122** (9), 1715–1741.

LEIBOVICH, S. 1977 On the evolution of the system of wind drift currents and Langmuir circulations in the ocean. Part 1. Theory and averaged current. *J. Fluid Mech.* **79** (4), 715–743.

LEIGHTON, R.I., SWEAN, J.F., HANDLER, R.A. & SWEARINGEN, J.D. 1991 Interaction of vorticity with a free surface in turbulent open channel flow. In *29th Aerospace Sciences Meeting*, p. 236. AIAA.

MARUSIC, I., MATHIS, R. & HUTCHINS, N. 2010 High Reynolds number effects in wall turbulence. *Intl J. Heat Fluid Flow* **31**, 418–428.

MEI, C.C., STIASSNIE, M. & YUE, D.K.P. 2005 *Theory and Applications of Ocean Surface Waves*. World Scientific.

MONTY, J.P., STEWART, J.A., WILLIAMS, R.C. & CHONG, M.S. 2007 Large-scale features in turbulent pipe and channel flows. *J. Fluid Mech.* **589**, 147–156.

NAKAGAWA, H. & NEZU, I. 1977 Prediction of the contributions to the Reynolds stress from bursting events in open-channel flows. *J. Fluid Mech.* **80** (1), 99–128.

NEZU, I. & NAKAGAWA, H. 1997 Space–time correlation structures of horizontal coherent vortices in compound open-channel flows by using particle tracking velocimetry. *J. Hydraul. Res.* **35** (2), 191–208.

NICHOLS, A., TAIT, S., HOROSHENKOV, K. & SHEPHERD, S. 2013 A non-invasive airborne wave monitor. *Flow Meas. Instrum.* **34**, 118–126.

OLSSON, P.J. & HENNINGSON, D.S. 1995 Optimal disturbance growth in watertable flow. *Stud. Appl. Maths* **94** (2), 183–210.

PAN, Y. & BANERJEE, S. 1995 A numerical study of free-surface turbulence in channel flow. *Phys. Fluids* **7** (7), 1649–1664.

PERUZZI, C., POGGI, D., RIDOLFI, L. & MANES, C. 2020 On the scaling of large-scale structures in smooth-bed turbulent open-channel flows. *J. Fluid Mech.* **889**, A1.

PERUZZI, C., VETTORI, D., POGGI, D., BLONDEAUX, P., RIDOLFI, L. & MANES, C. 2021 On the influence of collinear surface waves on turbulence in smooth-bed open-channel flows. *J. Fluid Mech.* **924**, A6.

PINELLI, M., HERLINA, H., WISSINK, J.G. & UHLMANN, M. 2022 Direct numerical simulation of turbulent mass transfer at the surface of an open channel flow. *J. Fluid Mech.* **933**, A49.

PIROZZOLI, S. 2023 Searching for the log law in open channel flow. *J. Fluid Mech.* **971**, A15.

PUJALS, G., GARCÍA-VILLALBA, M., COSSU, C. & DEPARDON, S. 2009 A note on optimal transient growth in turbulent channel flows. *Phys. Fluids* **21** (1), 015109.

RASHIDI, M. 1997 Burst-interface interactions in free surface turbulent flows. *Phys. Fluids* **9** (11), 3485–3501.

RASHIDI, M. & BANERJEE, S. 1988 Turbulence structure in free-surface channel flows. *Phys. Fluids* **31** (9), 2491–2503.

REYNOLDS, W.C. & HUSSAIN, A.K.M.F. 1972 The mechanics of an organized wave in turbulent shear flow. Part 3. Theoretical models and comparisons with experiments. *J. Fluid Mech.* **54** (2), 263–288.

SAMANTA, A. 2020 Non-modal stability analysis in viscous fluid flows with slippery walls. *Phys. Fluids* **32** (6), 064105.

SCHMID, P.J. 2007 Nonmodal stability theory. *Annu. Rev. Fluid Mech.* **39**, 129–162.

SCHMID, P.J. & HENNINGSON, D.S. 2001 *Stability and Transition in Shear Flows*. Springer.

SHEN, L., TRIANTAFYLLOU, G.S. & YUE, D.K.P. 2000 Turbulent diffusion near a free surface. *J. Fluid Mech.* **407**, 145–166.

SHEN, L., ZHANG, X., YUE, D.K.P. & TRIANTAFYLLOU, G.S. 1999 The surface layer for free-surface turbulent flows. *J. Fluid Mech.* **386**, 167–212.

SHEN, Y., YANG, S. & LIU, J. 2023 Characteristics of very large-scale motions in rough-bed open-channel flows. *Water* **15**, 1433.

SHRESTHA, K., ANDERSON, W., TEJADA-MARTÍNEZ, A.E. & KUEHL, J. 2019 Orientation of coastal-zone Langmuir cells forced by wind, wave and mean current at variable obliquity. *J. Fluid Mech.* **879**, 716–743.

SONG, Y., HUANG, W.X. & XU, C.X. 2017 Effect of active control on linear transient growth in turbulent channel flow. *J. Turbul.* **18**, 203–218.

SONG, Y., XU, C.X., HUANG, W.X. & CUI, G.X. 2015 Optimal transient growth in turbulent pipe flow. *Appl. Math. Mech.* **36**, 1057–1072.

TAMBURRINO, A. & GULLIVER, J.S. 2007 Free-surface visualization of streamwise vortices in a channel flow. *Water Resour. Res.* **43** (11), 1–12.

TEJADA-MARTÍNEZ, A.E., AKAN, C., SINHA, N., GROSCH, C.E. & MARTINAT, G. 2013 Surface dynamics in LES of full-depth Langmuir circulation in shallow water. *Phys. Scr.* **2013** (T155), 014008.

TEJADA-MARTÍNEZ, A.E. & GROSCH, C.E. 2007 Langmuir turbulence in shallow water. Part 2. Large-eddy simulation. *J. Fluid Mech.* **576**, 63–108.

TREFETHEN, L.N., TREFETHEN, A.E., REDDY, S.C. & DRISCOLL, T.A. 1993 Hydrodynamic stability without eigenvalues. *Science* **261** (5121), 578–584.

TRIANTAFYLLOU, G.S. & DIMAS, A.A. 1989 Interaction of two-dimensional separated flows with a free surface at low Froude numbers. *Phys. Fluids* **1** (11), 1813–1821.

WANG, G. & RICHTER, D.H. 2019 Two mechanisms of modulation of very-large-scale motions by inertial particles in open channel flow. *J. Fluid Mech.* **868**, 538–559.

WILLIS, A.P., HWANG, Y. & COSSU, C. 2010 Optimally amplified large-scale streaks and drag reduction in turbulent pipe flow. *Phys. Rev.* E **82**, 036321.

YIH, C.S. 1972 Surface waves in flowing water. *J. Fluid Mech.* **51** (2), 209–220.

YOSHIMURA, H. & FUJITA, I. 2020 Investigation of free-surface dynamics in an open-channel flow. *J. Hydraul. Res.* **58** (2), 231–247.

ZAMPIRON, A., CAMERON, S. & NIKORA, V. 2020 Secondary currents and very-large-scale motions in open-channel flow over streamwise ridges. *J. Fluid Mech.* **887**, A17.